Research article

Cytotoxicity of green synthesized zinc oxide nanoparticles using *Musa acuminata* on Vero cells

Harshyini Maheswaran [a], Sinouvassane Djearamane [a,d,*], Anto Cordelia Tanislaus Antony Dhanapal [b], Ling Shing Wong [c]

[a] *Department of Biomedical Sciences, Faculty of Science, Universiti Tunku Abdul Rahman (UTAR), Kampar Campus, Jalan Universiti, Bandar Barat, 31900, Kampar, Perak, Malaysia*
[b] *Department of Chemical Science, Faculty of Science, Universiti Tunku Abdul Rahman (UTAR), Kampar Campus, Jalan Universiti, Bandar Barat, 31900, Kampar, Perak, Malaysia*
[c] *Faculty of Health and Life Sciences, INTI International University, Persiaran Perdana BBN, Putra Nilai, 71800, Nilai, Negeri Sembilan, Malaysia*
[d] *Biomedical Research Unit and Lab Animal Research Centre, Saveetha Dental College, Saveetha Institute of Medical and Technical Sciences, Saveetha University, Chennai, 602 105, India*

ARTICLE INFO

ABSTRACT

Zinc oxide nanoparticles (ZnO NPs) have become a highly regarded substance in various industries especially biologically synthesized ZnO NPs due to their adherence to the principles of green chemistry. However, concerns have been raised regarding the potential cytotoxic effects of ZnO NPs on biological systems. This study aimed to investigate and compare the cytotoxicity of ZnO NPs that were synthesized through chemical (C–ZnO NPs) and green approach using *Musa acuminata* leaf aqueous extract (Ma-ZnO NPs) on Vero cells.

Characterization of ZnO NPs through Uv–Vis, FESEM, EDX, XRD, FTIR and XPS confirmed the successful synthesis of C- and Ma-ZnO NPs. MTT and ROS assays revealed that C- and Ma-ZnO NPs induced a concentration- and time-dependent cytotoxic effect on Vero cells. Remarkably, Ma-ZnO NPs showed significantly higher cell viability compared to C–ZnO NPs. The corelation of ROS and vell viability suggest that elevated ROS levels can lead to cell damage and even cell death. Flow cytometry analysis indicated that Ma-ZnO NPs exposed cells had more viable cells and a smaller cell population in the late and early apoptotic stage. Furthermore, more cells were arrested in the G1 phase upon exposure to C–ZnO NPs, which is associated with oxidative stress and DNA damage caused by ROS generation, proving its higher cytotoxicity than Ma-ZnO NPs. Similarly, time-dependent cytotoxicity and morphological alterations were observed in C- and Ma-ZnO NPs treated cells, indicating cellular damage. Furthermore, fluorescence microscopy also demonstrated a time-dependent increase in ROS formation in cells exposed to C- and Ma-ZnO NPs.

In conclusion, the findings suggest that green ZnO NPs possess a favourable biocompatibility profile, exhibiting reduced cytotoxicity compared to chemically synthesized ZnO NPs on Vero cells. These results emphasize the potential of green synthesis methods for the development of safer and environmentally friendly ZnO NPs.

---

* Corresponding author. Department of Biomedical Sciences, Faculty of Science, Universiti Tunku Abdul Rahman (UTAR), Kampar Campus, Jalan Universiti, Bandar Barat, 31900, Kampar, Perak, Malaysia.
E-mail address: sinouvassane@utar.edu.my (S. Djearamane).

1. Introduction

Over the last decade, research on nanomaterial-based products has created great excitement due to improved performance and functionality. Nanotechnology is the design, characterization, manufacture, and implementation of structures, devices, and systems at the nanometre scale by regulating their shape and size. Generally, the nanoparticle is a particle of 100 nm or less in size, and there is an enormous difference between its properties and those of the same material at larger scales [1,2].

Zinc oxide nanoparticles (ZnO NPs) have attracted interest for numerous different applications due to their distinctive and unique properties, such as electrical, thermal and optical [3,4]. Other properties of ZnO NPs include strong chemical stability, high photo-stability and high electrochemical coupling coefficient but most importantly their biocompatibility and biodegradability features make them a material of significant value for biomedical purposes [5,6].

ZnO NPs have been investigated for their ability to act as antibacterial agents in food packaging, effectively inhibiting and eradicating both common and significant foodborne pathogens [7,8]. The utilization of ZnO NPs have facilitated seed germination, enhanced seedling vigor, and promoted overall plant growth. Additionally, this nanoscale treatment was found to be beneficial in augmenting both stem and root development in peanuts [9]. ZnO NPs are also incorporated into ointments, creams, and lotions to shield the skin from sunburn and UV damage, offering broad-spectrum protection against UVA and UVB rays [10]. Some studies have also shown that ZnO-NPs are effective on cancer cells [11] surpassing the therapeutic effectiveness of certain conventional chemotherapy drugs in comparable ex vivo investigations [12].

Nanoparticles can be synthesized through two approaches which are bottom-up and top-down approaches [13,14]. Although physical and chemical methods have high-yield production [15], they use reductants and stabilizing agents that are destructive to the environment, produce a high amount of impurities, are expensive and time-consuming [16]. Currently, the biological synthesis methods also known as "Green synthesis" for NPs are capturing attention. This method aims to cut the usage of chemicals as a step forward to create an eco-friendly route in synthesizing ZnO NPs. Microorganism, and plant parts such as flower, stem, and leaf are the common materials employed for green synthesis method [17].

Banana is among the oldest crops grown in human agriculture history, and *M. acuminata*, a widely cultivated variety, has played a significant role in global food cultures. The source of this specific plant family ranges from India to Papua New Guinea, which encompasses the area of Southeast Asia [18]. India continues to be the world's biggest banana producer, accounting for greater than 25 % of global banana production and Malaysia is ranked 12th in Asia [19]. A significant quantity of waste is produced by banana cultivation. The fruit represents only about 12 % of the plant by weight and the residual sections become agricultural waste [20]. The leaves are large, cheap, and easily available throughout the year which makes it a sustainable plant part to be used in biomedical research such as green nanoparticle synthesis [21].

With the growing uses of ZnO NPs, exposure to it is higher in this day and age and there is a need for further research to fully understand the potential adverse effects of ZnO NPs on human health. Excessive exposure to ZnO NPs may lead to adverse health effects like skin irritation. However, the FDA considers zinc oxide to be a harmless metal oxide that can be safely used [22]. Existing literature does not provide a comprehensive understanding of the extent and consequences of exposure to ZnO NPs, particularly in relation to the safe dose. Therefore, caution should be exercised when using ZnO NPs and further research is needed to fully understand their properties and potential risks.

Furthermore, there is a research gap regarding the comparison between green synthesized ZnO NPs and chemically synthesized ones. While the advantages of green synthesis, such as adhering to the principles of green chemistry and transforming waste into beneficial products, are acknowledged, there is a lack of studies that specifically explore the potential of *M. acuminata* leaves aqueous extract green-synthesized ZnO NPs for safer and more sustainable applications. Closing these research gaps will contribute to the literature on the safe doses of ZnO NPs and provide insights into the potential benefits of green synthesis in ZnO NPs production.

Vero cells were chosen for this study because ZnO NPs are known to be eventually transported to the kidneys once inside the body, making them relevant for studying renal toxicity. Moreover, since various organs are interconnected within the human body, assessing the toxicity in kidney cells can also serve as a representative indicator for potential toxic effects on other organs. Other than that, Vero cells closely resemble human cell behaviour, allowing us to evaluate the toxicity of ZnO NPs both in animals and potentially in humans which makes it a reliable model for cytotoxicity study.

2. Methodology

2.1. M. acuminata leaf aqueous extract

Fresh leaves of *M. acuminata* were retrieved from Universiti Tunku Abdul Rahman's Agriculture Farm at Kampar. The leaves were rinsed using distilled H_2O and dried for four days in an oven at 50 °C before grounding into a fine powder. Then, 50 g of *M. acuminata* leaf powder was placed into 1000 mL of distilled H_2O and left for 24 h. The solution was filtered using a muslin cloth and centrifuged for 10 min at 7000 rpm. The aqueous extract was freeze-dried to obtain the crude extract which was stored at −20 °C.

2.2. Phytochemical analysis of M. acuminata leaf extract

The incorporation of phytochemical analysis in this study was to explore of the bioactive compounds present in the aqueous extract.

2.2.1. Test for coumarins

To 2 mL of extract, 10 % of 1 mL sodium hydroxide (NaOH) was added. Hydroxycoumarin was used as a standard. The development of yellow shows the presence of coumarins.

2.2.2. Test for flavonoids

To 1 mL of extract, 5 drops of 20 % NaOH and 5 drops of 0.1 M hydrochloric acid (HCl) were added. Quercetin was used as a standard. The presence of yellow which turned colourless specified the presence of flavonoids.

2.2.3. Test for phenols

To 1 mL of extract, 5 drops of 5 % ferric chloride (FeCl$_3$) were added. Gallic acid acted as the standard. Black colouration showed the existence of phenols.

2.2.4. Test for quinones

To 1 mL of extract, 5 drops of concentrated sulphuric acid (H$_2$SO$_4$) were added. Plumbagin was used as a standard. The appearance of red colour demonstrated the presence of quinones.

2.2.5. Test for saponins

To 1 mL of extract, 4 mL of distilled H$_2$O was added to the test tube which was then vigorously shaken for 3 min. Saponin was used as a standard. The existence of saponins was determined by the production of stable foam.

2.2.6. Test for tannins

To 1 mL of extract, 3 drops of 10 % FeCl$_3$ were added. Tannic acid was used as a standard. The presence of phenols and tannins was determined by the presence of a green-black colouration.

2.3. DPPH assay

The antioxidant potential of the aqueous extract was assessed through a DPPH assay. The aqueous extract, ascorbic acid, and DPPH solution were dissolved separately in methanol to get 2 mg/mL. The serial dilutions of the aqueous extract and ascorbic acid were prepared at concentrations of 100 to 0.05 μg/mL. Then, a volume of 10 μL of DPPH solution was introduced into every well and were kept for 30 min at room temperature in the dark. After the incubation time, the absorbance was measured at 517 nm. Ascorbic acid was used as the standard. The scavenging capacity was calculated based on the formula:

$$\text{Percentage of radical scavenging activity}\left(\%\right) = \frac{(A_o - A_s)}{A_o} \times 100\%$$

where A_0 is the negative control (methanol and DPPH solution) absorbance and A_s is the absorbance of the sample.

2.4. ZnO NPs synthesis

To synthesize ZnO NPs through chemical and green synthesis approach, firstly, 0.4 mol of NaOH and 200 mg of *M. acuminata* crude extract in 30 mL of distilled H$_2$O were prepared separately, respectively. Under continuous stirring, 0.2 mol of Zn(NO$_3$)$_2$•6H$_2$O was added dropwise into each beaker. The milky white (chemical synthesis) and light green (green synthesis) solutions were left to stir for 2 h, respectively. Then, both the solutions were centrifuged at 8000 rpm for 10 min. The supernatants were decanted and the precipitates were rinsed twice with distilled H$_2$O and ethanol. Lastly, the pellets were both calcined at 400 °C for 2 h to obtain a white and light yellowish powder, through chemical and green synthesis, respectively.

2.5. Characterization of ZnO NPs

The structural and morphological characteristics of the synthesized ZnO NPs were explored using a range of analytical techniques.

2.5.1. UV–Vis spectrometry (UV–Vis)

A tiny amount of the nanopowder was re-suspended in around 10 mL of de-ionized H$_2$O and placed into a 1 cm path quartz cell to assess the optical properties of both chemical and green synthesized ZnO NPs. It was then scanned from 200 to 700 nm using a UV-Spectrophotometer (Shimadzu UV-1700, Tokyo, Japan) and the highest absorbance was measured.

The optical band gap (E_g) was calculated using Tauc's equation as follows:

$$\alpha h\nu = A\left(h\nu - E_g\right)^2$$

where $h\nu$ = photon energy, E_g=optical energy bandgap, A = band tailing parameter (constant) and α = absorption coefficient.

2.5.2. Field emission scanning electron microscopy (FESEM)

The structure and morphology of the synthesized ZnO NPs were analysed using Sigma VP (Zeiss) with an acceleration voltage of

2.5–2.8 keV machine. By adding a tiny amount of ZnO NPs onto the carbon-coated tape, a thin layer of ZnO NPs was created and the thin film was left to dry. Then, the sample was subjected for FESEM analysis.

2.5.3. Energy-dispersive X-ray spectroscopy (EDX)

EDX (X-max50, Oxford) was used to determine and quantify the elemental composition, chemical purity and stoichiometry of synthesized ZnO NPs.

2.5.4. X-ray diffraction (XRD)

The crystal phase compositions of both the ZnO NPs were investigated using x-ray diffraction SHIMADZU, XRD-6000, Japan with the following parameters: Cu-Kα radiation (1.5406 Å), operating voltage—40 kV, current 30 mA, in the scan range $10 \leq 2\theta \leq 80°$, step 0.02°. Debye-Scherrer's formula was used to calculate crystallite sizes as follows:

$$\text{Debye} - \text{Scherrer equation} : D = \frac{k\lambda}{\beta \cos \theta}$$

where D is the crystallite size (nm), k is a constant (0.94 for spherical particles), λ is the X-ray wavelength for Cu Kα radiation (Cu-Kα = 0.1541 nm), β is the full width at half-maximum (FWHM) [rad] and θ is Bragg diffraction angle in degree.

2.5.5. Fourier transform infrared spectroscopy (FTIR)

The chemically and green synthesized ZnO NPs powder were mixed thoroughly with potassium bromide (KBr) separately until a homogenous powder was formed. The sample was then compressed using a hydraulic press to form a compact pellet. The FTIR spectra were acquired over a range of $4000-400 \text{ cm}^{-1}$ on an FT-IR PerkinElmer Spectrophotometer.

2.5.6. X-ray photoelectron spectroscopy (XPS)

X-ray photoelectron spectroscopy (XPS) was done on C- and Ma- ZnO NPs powder (AXIS Ultra equipped with DLD, Kratos Analytical, Manchester, UK) using low-resolution survey scans (1 eV step, 80 eV CAE) to identify element surface compositions, while carbon high-resolution sections (0.1 eV step, 20 eV CAE) were used for chemical characterization. Every sample was analysed from three different points (the analysis area was nominally 400 × 800 mm).

2.6. Cell culture

The Vero cell line (CCL-81), acquired from the American Tissue Culture Collection (ATCC, USA), was utilised as a model for the normal cell line. The cells were grown in Dulbecco's Modified Eagle's Medium (DMEM) supplemented with 10 % Fetal Bovine Serum (FBS) and were kept in a 5 % CO_2 incubator at 37 °C. The culture medium was replaced two times per week and the cells were sub-cultured using trypsin-ethylenediamine tetra acetic acid (EDTA) once a week.

2.7. Treatment of ZnO NPs onto Vero cells

The master stock for C–ZnO NPs and Ma-ZnO NPs was prepared in DMEM at a concentration of 5 mg/mL, separately. A 0.22 m syringe filter was then used to filter the stock solution. Then, working solutions of 200 μg/mL were prepared in DMEM from the master stocks of C–ZnO NPs and Ma-ZnO NPs. The Vero cells were seeded into a flat-bottomed 96-well and after 24 h of incubation, serial dilution of the working solution was done to achieve concentrations of 0.05, 0.10, 0.20, 0.39, 0.78, 1.56, 3.13, 6.25, 12.50, 25.00, 50.00, and 100.00 μg/mL. In 100 μl of growth medium, an untreated cell population was used as the negative control. The cells were then incubated for 24, 48, and 72 h in a 5 % CO_2 incubator at 37 °C before being subjected to cytotoxicity assay, oxidative stress assessment and flow cytometry.

2.8. In vitro cytotoxicity evaluation of ZnO NPs on Vero cells

2.8.1. MTT assay

MTT assay is a rapid tetrazolium salt-based colorimetric assay with pertinence for the estimation of metabolic activity of viable cells. After 24, 48, and 72 h incubation of cells treated with C– ZnO NPs and Ma-ZnO NPs, 20 μl of MTT dye (Invitrogen, Molecular Probes Inc., USA) was applied to each well and the plates underwent incubation in the dark at 37 °C for 4 h in a 5 % CO_2 incubator. Following this incubation period, the media was aspirated and 100 μl of DMSO was introduced to dissolve the formazan crystals. Fifteen mins later, the colour intensity of the wells was measured against a blank reagent at 550 nm by a microplate reader (Bio-Rad Laboratories, Hercules, CA, USA). Serial dilution of DMSO starting at 100 % was used as the positive control. The equation below was used to enumerate the percentage of cellular viability with respect to the negative control:

$$\text{Cellular viability } (\%) = \frac{\text{Absorbance of treated cells}}{\text{Absorbance of negative control}} \times 100$$

2.8.2. ROS assay

2′-7′-dichlorodihydrofluorescein diacetate (DCFH-DA) is an intracellular fluorescent probe that is often employed in cellular studies

to measure the redox state of a cell. Firstly, the DCFH-DA stock solution of 10 mM was concocted in 1 mL of DMSO and a working solution of 10 μM was prepared by diluting the stock solution 1000-fold in DMEM. After incubation of cells with C– ZnO NPs and Ma-ZnO NPs, the cells were rinsed once with 1× PBS to dispose of the remaining ZnO NPs and medium. Then, 100 μl of the 2′,7′-dichlorodihydrofluorescein diacetate (H_2DCF-DA) (Invitrogen, Molecular Probes Inc., USA) working solution was introduced to every well and the plates were kept in the dark at 37 °C in a 5 % CO_2 incubator for 30 min. Subsequently, the cells were washed again to remove any excess probe. PBS was added to the stained cells and the cytosolic green fluorescence intensity was quantified through a fluorescent microplate reader (Bio-Rad Laboratories, Hercules, CA, USA) at wavelengths of 485 nm excitation and 530 nm emission. The positive control cells were exposed to 1 mM hydrogen peroxide. The equation below calculated the percentage of increase in ROS with respect to the negative control:

$$\text{Percentage of increase in ROS } (\%) = \frac{\text{Fluorescence of treated cells}}{\text{Fluorescence of negative control}} \times 100$$
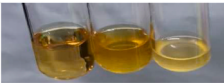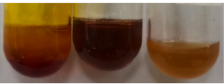
2.8.3. Flow cytometry

Flow cytometry is a rapid method for analysing large numbers of individual cells using light-scattering and fluorescence where it provides morphological and spatial information at single-cell resolution. After exposing Vero cells to 100 μl of C- and Ma-ZnO NPs for 72 h, the treatments were removed by washing the cells with 100 μl of 1× PBS. Next, the cells were harvested by trypsinization and collected, followed by centrifugation at 300g for 5 min. The cells were washed and centrifuged once more. The cells were thereafter resuspended in 500 μl of binding buffer and subsequently by the dyes, 5 μl of Annexin V-FITC and 7AAD which were incubated for 10 min in dark. Then, the cells were loaded into the Attune NxT Acoustic Focusing flow cytometer (Thermo Fisher Scientific, USA). Two negative controls were used for this analysis. The first was the unstained sample and the second negative control was stained with 5 μl of both dyes. The positive control cells were treated with 100 μl of DMSO. A sum of 10,000 events was analysed for each sample. Flow cytometry data analysis for viability and cell cycle was performed by FlowJo software (Version 10.8.1).

2.9. Microscopic analysis of ZnO NPs on Vero cells

A 6-well culture plate was used to investigate the microscopic analysis of C–ZnO NPs as well as Ma-ZnO NPs on Vero cells for 24, 48 and 72 h at 100.00 μg/mL.

Table 1
Phytochemical analysis of *M. acuminata* leaf aqueous extract.

Phytochemical Analysis	Presence	Observation (Standard, Aq. Ex., NC)
Coumarins	++	
Flavonoids	+	
Phenols	++	
Quinones	+++	
Saponins	+++	
Tannins	++	

Keys.
[+] Present in low concentration.
[++] Present in moderate concentration.
[+++] Present in high concentration.

2.9.1. Inverted microscopy

The possible cellular morphological changes of Vero cells upon exposure to C–ZnO NPs and Ma-ZnO NPs were determined through a Nikon ECLIPSE Ti–S inverted microscope (Tokyo, Japan) at $10\times$ magnification.

2.9.2. Fluorescence microscopy

The qualitative analysis of ROS generation on Vero cells exposed to C–ZnO NPs and Ma-ZnO NPs was visualized using an inverted fluorescence microscope (Nikon ECLIPSE Ti–S, Tokyo, Japan).

2.10. Statistical analysis

Statistical analysis was conducted to examine the variance and ensure the reliability of the in vitro tests involving Vero cells and the exposure to C–ZnO NPs and Ma-ZnO NPs. All experiments were performed in triplicates (n = 3) to account for experimental variability and enhance the validity of the results. The data obtained from these experiments were represented as the mean. One-way analysis of variance (ANOVA) was employed in SPSS 22 software, and the significance level was fixed at $p < 0.05$. In succession, Tukey and Dunnet's T3 post hoc test was used for multiple comparisons.

3. Results and discussion

3.1. M. acuminata leaf aqueous extract analysis

3.1.1. Phytochemical study

The phytochemicals present (+) in the aqueous extract of *M. acuminata* leaf are demonstrated in Table 1.

3.1.2. DPPH assay

DPPH (2,2-diphenyl-1-picryl-hydrazyl-hydrate) is a stable free radical and commercially available organic nitrogen radical, which reacts with electron donor compounds. The delocalization of the spare electron gives rise to the deep violet colour [23–25]. *M. acuminata* leaf aqueous extract was screened for its antioxidant activity through DPPH assay. Fig. 1 shows the antiradical curve that was plotted pertaining to the concentration of the aqueous extract and ascorbic acid on the x-axis while its comparative scavenging activity on the y-axis. The graph indicated that the aqueous extract significantly hindered the formation of free radicals depending on the concentrations. The DPPH scavenging activity improved proportionately with the aqueous extract quantity. The EC_{50} of aqueous extract and ascorbic acid was estimated to be 7.3 µg/mL and 0.028 µg/mL, consecutively.

3.2. Synthesis of zinc oxide nanoparticles

3.2.1. Visual observation of ZnO NPs formation

Visual characterization is the preliminary test to confirm ZnO NPs synthesis. $Zn(NO_3)_2 \bullet 6H_2O$, a colourless solution was used as the precursor in both chemical and green synthesis methods. In chemical synthesis process, colourless NaOH was added which resulted in a milky white suspension as illustrated in Fig. 2. On the contrary, in the green synthesis of ZnO NPs, a clear dark brownish-green
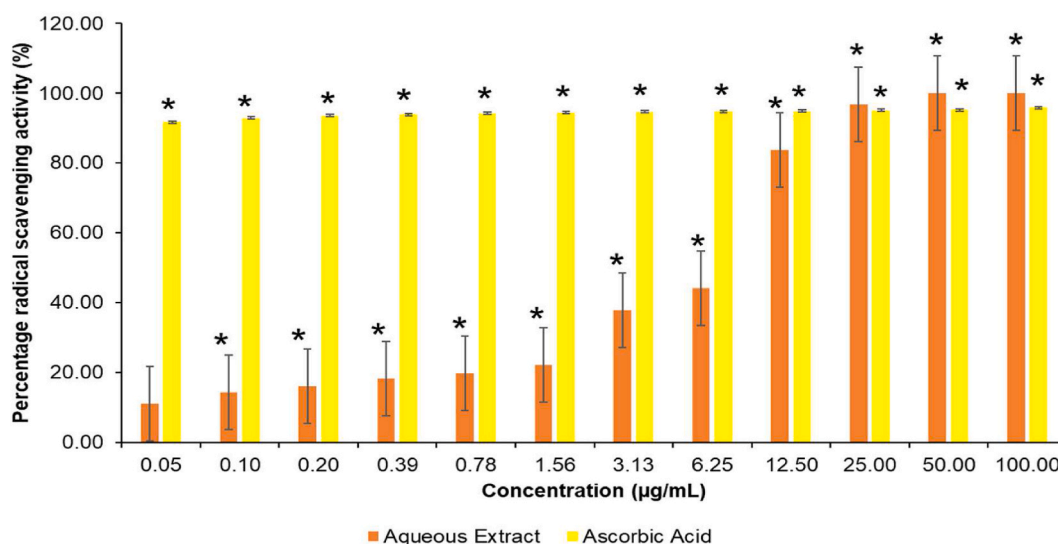

Fig. 1. DPPH assay of *M. acuminata* leaf aqueous extract.

M. acuminata leaf aqueous extract was used which produced a whey colour suspension as shown in Fig. 3.

The colour intensity of the suspensions developed as time progressed, revealing that zinc ions are continuously reduced. Within the hour, the colour of both the solutions stopped changing which signalled the complete reduction of zinc oxide. After calcination, chemical and green synthesis methods yielded C–ZnO NPs and Ma-ZnO NPs powder, respectively, with the former being white and the latter pale yellow. These results corroborated the visual inspection of ZnO NPs synthesis in previous literature [26,27]. About 2.03 g and 0.617 g of C–ZnO NPs and Ma-ZnO NPs were obtained after calcination, which gave the percentage yields of 53.70 % and 16.32 %, respectively.

3.2.2. Mechanism of C- and Ma- ZnO NPs synthesis

The mechanism of C- and Ma-ZnO NPs synthesis is presented in Fig. 4. The precipitation method used to synthesize C- and Ma-ZnO NPs is an example of the bottom-up approach to synthesize NPs [28] where zinc nitrate hexahydrate solution was used as the zinc precursor salt. NaOH and *M. acuminata* leaf aqueous extract acted as the precipitating agent. The phytochemical assay and DPPH assay results prove that there are phytocompounds present in the aqueous extract that aided in the biosynthesis of Ma-ZnO NPs. The phytocompounds are responsible for the biosynthesis of Ma-ZnO NPs that also act as stabilizing agents. Once the salt and base are mixed dropwise under constant stirring, it results in a white and pale yellow precipitate for C- and Ma-ZnO NPs respectively, that is insoluble in water which is zinc hydroxide ($Zn(OH)_2$). OH groups in the precipitating agents reduce the Zn cations to Zn^0 which results in the formation of $Zn(OH)_2$ [29,30]. Subsequently, the precipitate was exposed to thermal treatment at 400 °C to obtain ZnO NPs. During calcination, the water evaporates and as a consequence, $Zn(OH)_2$ is converted into ZnO [31].

3.3. Characterization of ZnO NPs

3.3.1. UV–Vis

UV–visible spectroscopy was used to investigate the transmittance spectra and optical properties of both synthesized ZnO NPs in the wavelength region of 200–700 nm. As shown in Fig. 5 (a and b), the absorption band recorded a characteristic absorption peak of C- and Ma-ZnO NPs at wavelengths of 371 nm and 360 nm respectively. This means that when the light at these wavelengths is shone on the NPs, they will absorb more of that light than at other wavelengths.

Fig. 5 (c and d) exhibits the plot $(\alpha h\nu)^2$ vs. $h\nu$ of the prepared ZnO NPs. The values of the energy band gap obtained for C- and Ma-ZnO NPs were 3.20 and 3.31 eV, respectively. When light with enough energy is absorbed by the NPs, an electron can be excited from the highest occupied electron energy level (the valence band) to the lowest unoccupied electron energy level (the conduction band). An energy band gap is a disparity in energy across the valence and conduction bands that allow for the conduction of electricity. With that said, the intrinsic band-gap absorbance of ZnO occurs between the valence band to the conduction band of O2p orbitals to the Zn3d orbitals [32].

3.3.2. SEM

SEM analysed the structure and morphology of C- and Ma-ZnO NPs. Fig. 6 (a – d) displays the SEM images of C- and Ma-ZnO NPs respectively which recognizes that both the ZnO NPs are nano-sized. The micrographs illustrated that both C- and Ma-ZnO NPs exhibited rod as well as truncated cubic-shaped NPs. In the SEM images of Ma-ZnO NPs, the NPs appear to be well distributed without aggregation. On the other hand, C–ZnO NPs seem to be composed of individual ZnO NPs and several aggregates.

3.3.3. EDX

The EDX spectrum of C- and Ma-ZnO NPs were verified in the spot-profile mode from one of the densely populated NPs areas as clearly illustrated in Fig. 7. The analysis revealed distinct peaks of zinc and oxygen atoms that confirm the formation of ZnO NPs in both samples. The spectra also indicated that both the synthesized ZnO NPs had partial purity. The elemental profile displayed a single peak of Zn and O at about 0.5 and 1 keV consecutively, as well as double peaks of Zn between 8 and 10 in both spectra. These data corroborate with previous studies of synthesized ZnO NPs where similar peaks were observed [33–36].

The percentages of the elements inset of Fig. 7 (a) reveal that zinc and oxygen comprised about 40.04 % and 40.76 % of C–ZnO NPs. Weak signals of carbon atoms were also recorded. The main reason for the presence of carbon in the sample could be due to the carbon
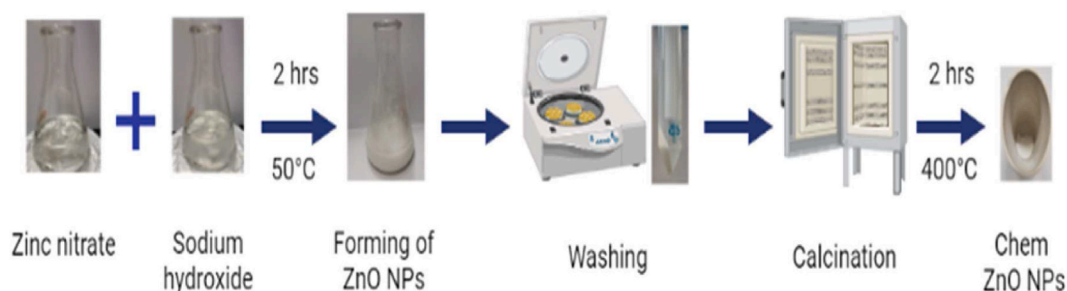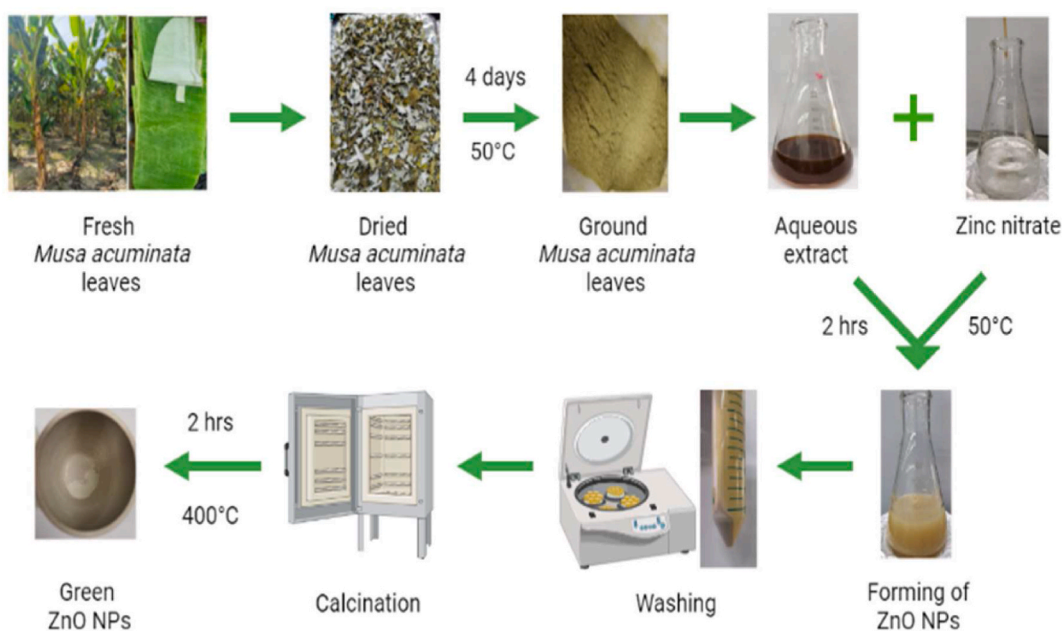

Fig. 2. Chemical synthesis of C–ZnO NPs.

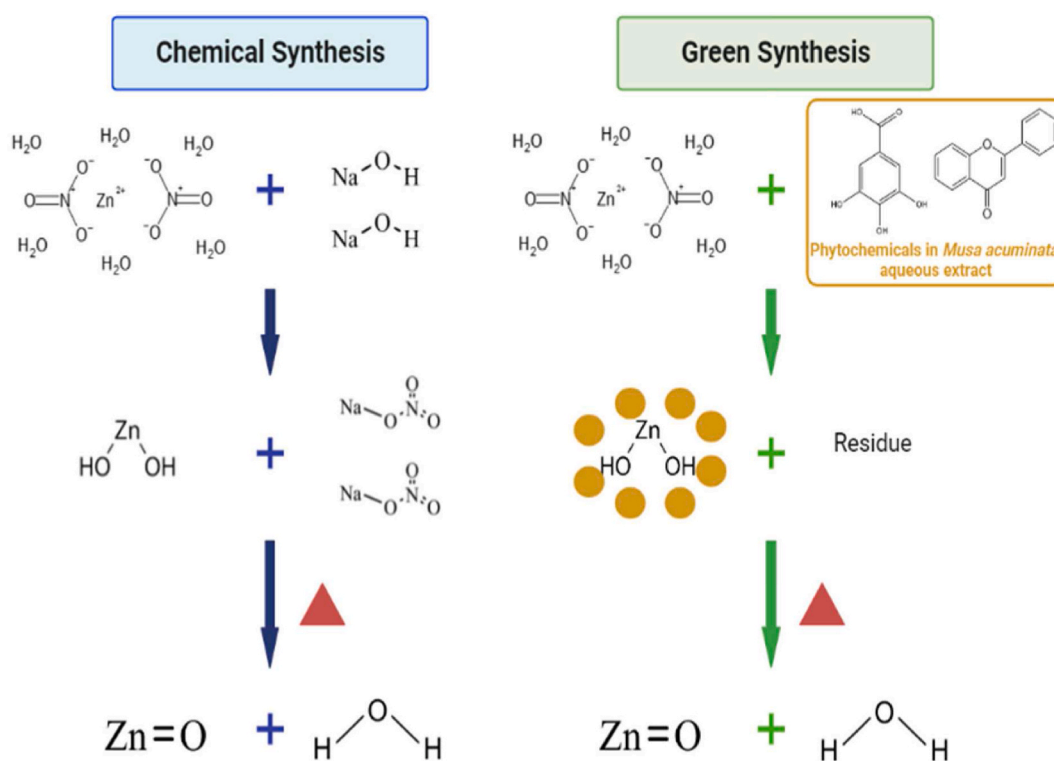**Fig. 3.** Green synthesis of Ma-ZnO NPs.

Fig. 4. Mechanism of synthesis of C- and Ma-ZnO NPs.

tape used in the procedure. EDX pattern displayed in Fig. 7 (b) indicates that the Ma-ZnO NPs are also composed of zinc and oxygen at about 38.53 % and 38.51 %. The percentage of elements showed slightly higher signals of carbon atoms in comparison to C–ZnO NPs. This could be due to the contribution of organic compounds from the aqueous extract that acted as a reducing agent in the green synthesis which could have introduced carbon into the final product.
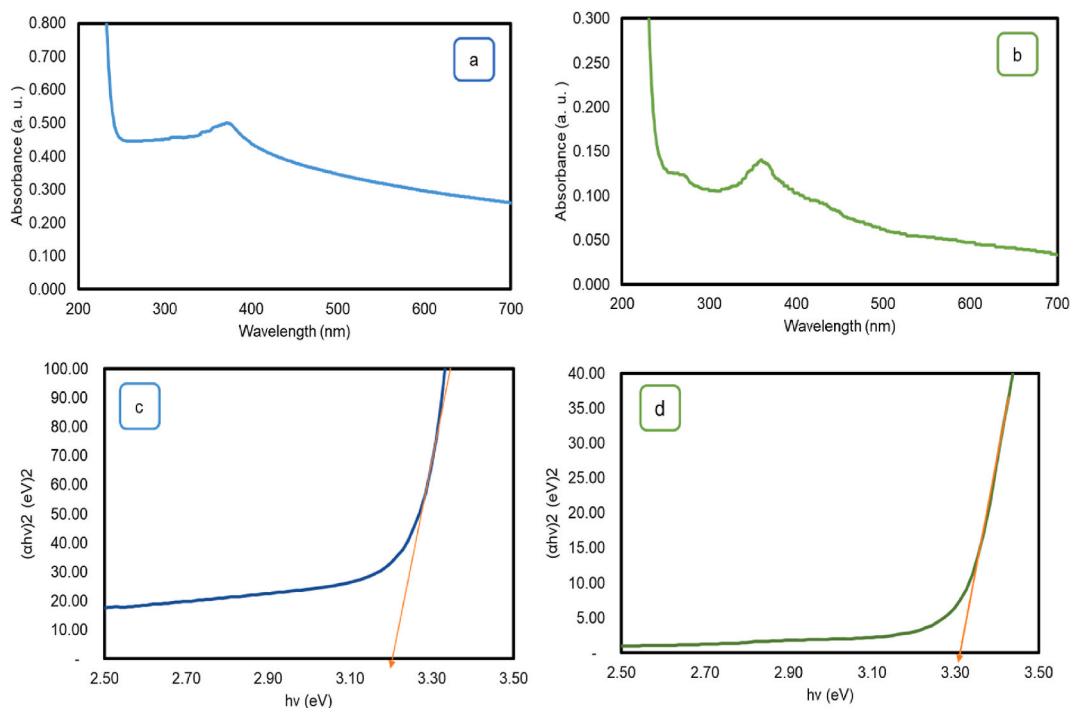
Fig. 5. Absorption peaks of (a) C–ZnO NPs and (b) Ma-ZnO NPs. Energy bandgaps of (c) C–ZnO NPs and (d) Ma-ZnO NPs in UV–Vis spectrum.
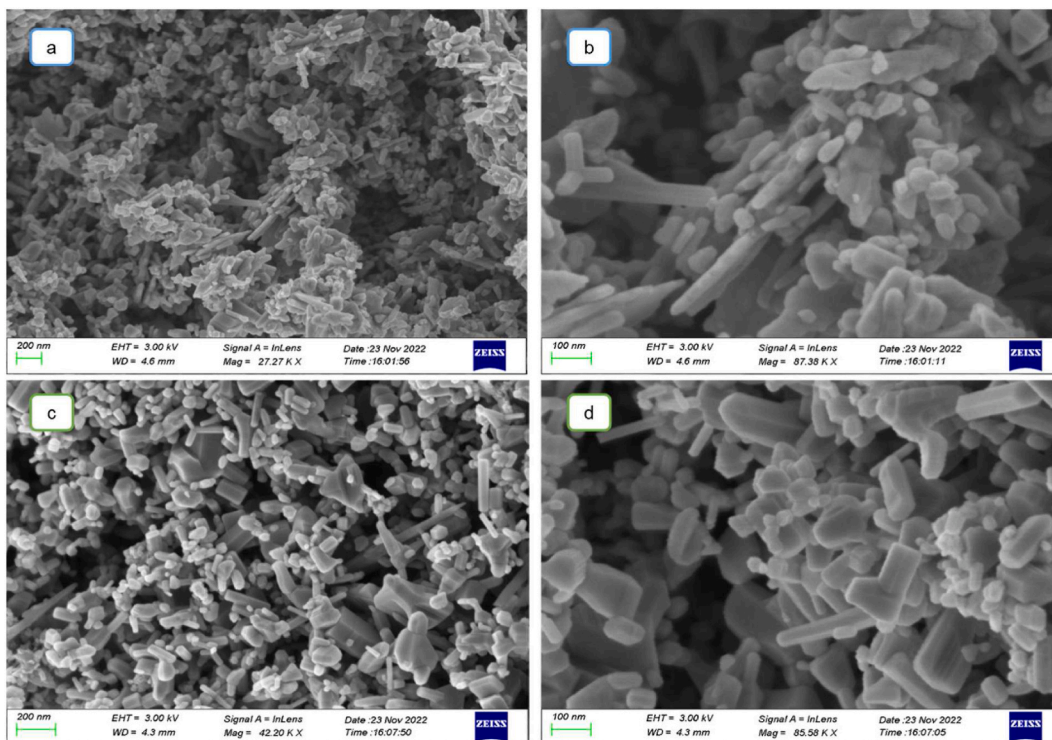

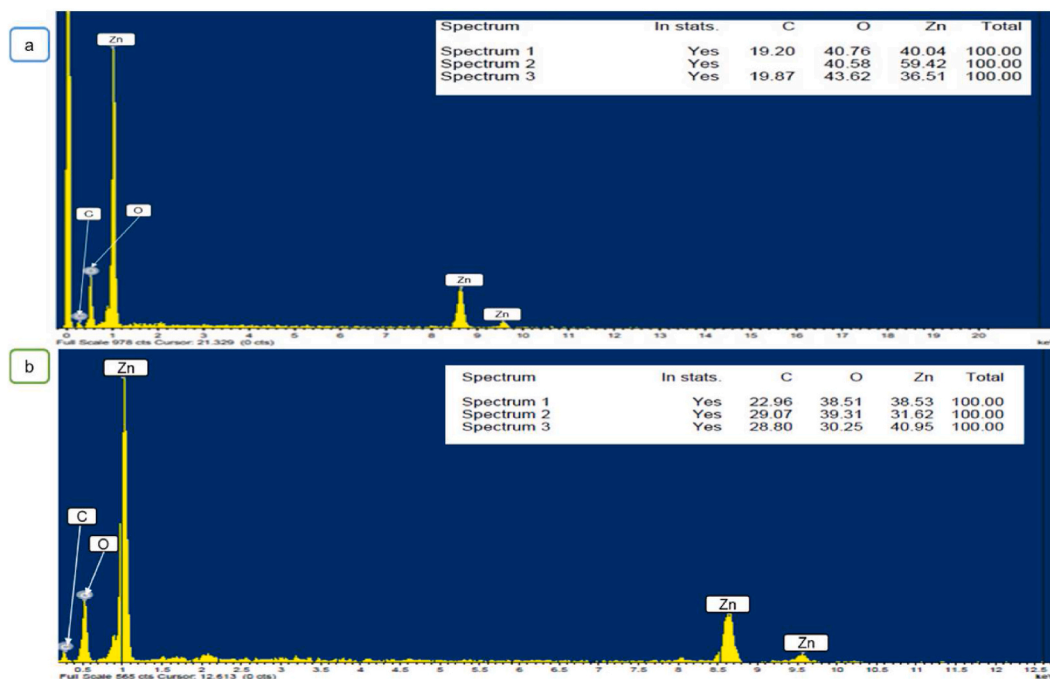**Fig. 6.** SEM images of (a and b) C–ZnO NPs and (c and d) Ma-ZnO NPs.

Fig. 7. EDX spectrum of (a) C–ZnO NPs and (b) Ma-ZnO NPs.

3.3.4. XRD

Fig. 8 (a) shows diffraction peaks of C–ZnO NPs at 31.78°, 34.44°, 36.27°, 47.56°, 56.62°, 62.88°, 66.41°, 67.98°, 69.11°, 72.60° and 76.99° in the spectra at diffraction lines (100), (002), (101), (102), (110), (103), (200), (112), (201), (004) and (202),
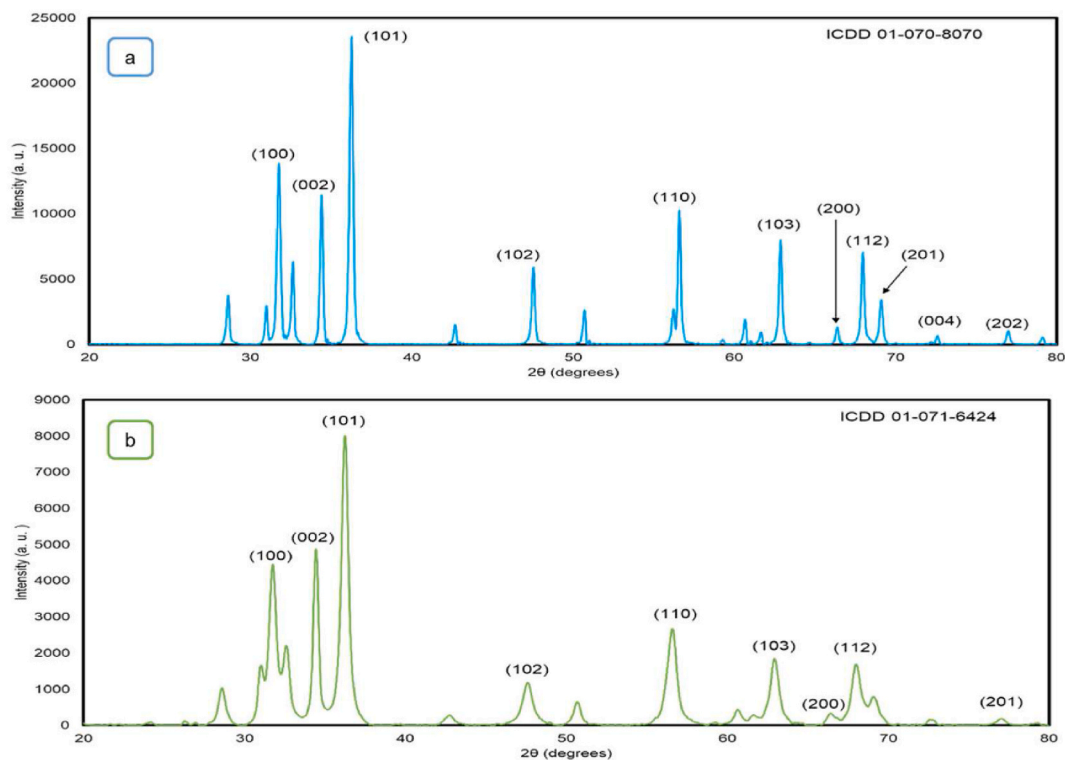

Fig. 8. XRD spectrum of (a) C–ZnO NPs and (b) Ma-ZnO NPs.

consequently. These findings are in good agreement with the peaks of the standard card file ICPD-01-070-8070 and are classified as ZnO hexagonal structures [37]. The XRD pattern of Ma-ZnO NPs includes the (100), (002), (101), (102), (110), (103), (200), (112), and (201) diffraction lines at 2θ values of 31.62°, 34.31°, 36.05°, 47.35°, 56.33°, 62.67°, 67.79°, 68.93°, 77.01° consecutively as shown in Fig. 8 (b). All of the detected diffraction peaks are in accordance with ICDD 01-071-6424, matching a hexagonal ZnO structure [38,39].

The cell constants of both ZnO NPs were a = 3.249 Å and c = 5.205 Å. The average crystallite size of C- and Ma-ZnO NPs were confirmed by Debye-Scherrer's equation and was estimated to be 41.96 nm and 21.87 nm respectively. C–ZnO NPs are found to be somewhat larger than MA-ZnO NPs which verifies the findings in SEM where some agglomeration was noted in C–ZnO NPs.

3.3.5. FTIR

The chemical structures of C- and Ma-ZnO NPs were analysed using the FT-IR spectroscopy technique as shown in Fig. 9 respectively. The peaks indicated the characteristics functional group present on the surface of the synthesized ZnO NPs which were studied from 4000 cm^{-1}–400 cm^{-1}. The FT-IR spectrum of C–ZnO NPs resulted in various peaks at 3436, 1633 and 530 cm^{-1}. The spectrum of Ma-ZnO NPs displayed the functional groups' bands at 3433, 1636, 1519, 1441, 1384, 919, 842 and 481 cm^{-1}. In the green synthesis of ZnO, several other functional groups are present around the NPs. The presence of signals for various functional groups established the contribution of phytocompounds from *M. acuminata* leaf aqueous extract that acted as precipitating as well as capping agents in the synthesis of Ma-ZnO NPs.

The apparent large peaks at 3436 and 3433 cm^{-1} match to the stretching vibration of hydroxyl (OH) groups from the water vapour in the air [40]. The peaks that were observed at 1633 and 1636 cm^{-1} are caused by the stretching of the C=O functional group from the atmospheric carbon dioxide [41,42]. Generally, metal oxides give absorption peaks in regions between 400 and 600 cm^{-1} [43]. Strong peaks seen at 530 and 481 cm^{-1} prominently indicate Zn–O stretching vibration and confirm the formation of ZnO NPs. These findings are in line with the literature values [27,40,44–46].

The other peaks found only in the spectrum of Ma-ZnO NPs were 1519, 1441, 1384, 919 and 842 cm^{-1}. The peak at 1519 cm^{-1} reveals the presence of the C=O amide II group. At 1441 cm^{-1}, the -C-H bending vibration band appears [40]. The absorption band at 1384 cm^{-1} correspond to C=O stretching of a carboxylic group and aromatic amine C–N stretching [47,48]. The peak at 919 cm^{-1} denotes the carboxylic acid (O–H) bending vibrations [48] and the = C–H bend arises at 842 cm^{-1} [49]. These peaks indicate phytocompounds content such as phenols, amines, carboxylic acids, aromatic amino acids and others that are present in the *M. acuminata* leaf aqueous extract. These functional groups interact with zinc and aid in the biosynthesis of ZnO NPs [43].

3.3.6. XPS

The elemental chemical states of C- and Ma-ZnO NPs were studied using the XPS technique. XPS spectra of C- and Ma-ZnO NPs are displayed in Fig. 10 shows the high-intensity peak of the elements Zn, O, as well as C. As evident in Fig. 11 (a) and Fig. 12 (a), the high-resolution XPS spectra show the characteristic Zn2p doublet peak. In both C- and Ma-ZnO NPs, the two strong peaks at a binding energy of 1023.2 and 1046.4 eV attribute to Zn $2p_{3/2}$ and Zn $2p_{1/2}$ consecutively, confirming the existence of the Zn element. The binding
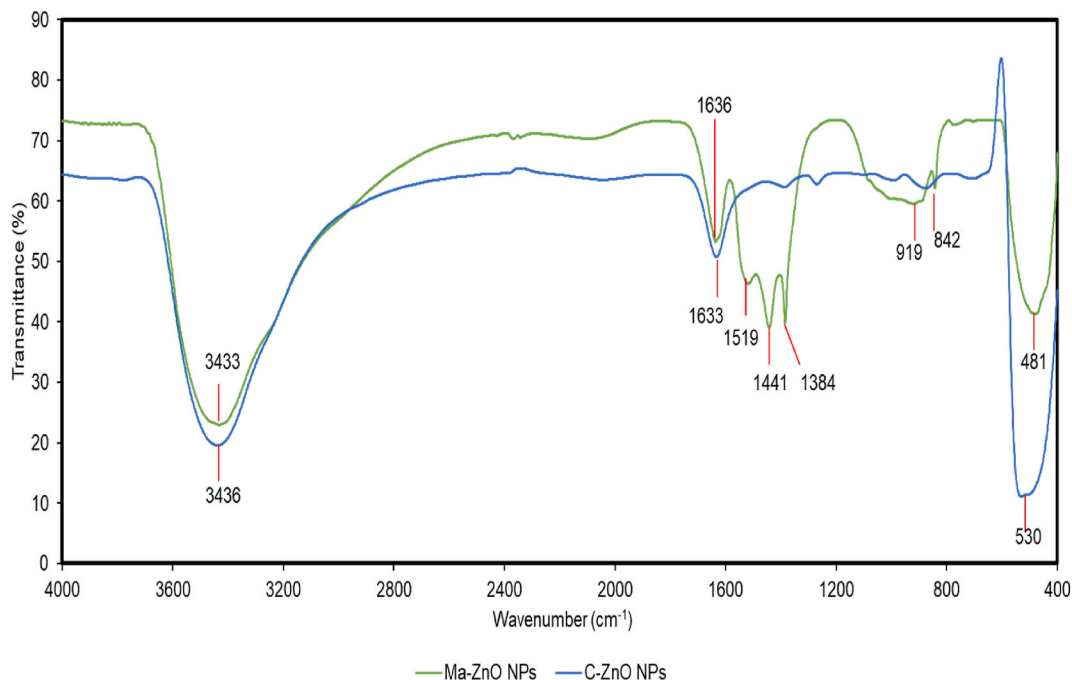

Fig. 9. FT-IR spectrum of C- (blue) and Ma-ZnO NPs (green).

energy difference between both peaks which was attributed to spin-orbit splitting was 23.2 eV, denoting the presence of zinc in the Zn^{2+} oxidation state [50–52].

Fig. 11 (b) Fig. 12 (b), portrays the O 1s spectra fitted by two peaks at 530.11 and 531.49 eV for C–ZnO NPs as well as 529.90 and 531.58 eV for Ma-ZnO NPs. The low binding energy peaks of 530.11 along with 529.90 eV represented the O^{2-} ions binding to Zn^{2+} ions within the wurtzite hexagonal phase of ZnO NPs [53,54]. The high binding energy peaks at 531.49 and 531.58 eV relate to the oxygen species on the surface as hydroxyl [50,55].

The XPS spectrum for C 1s Fig. 12 (c)was convoluted into triple peaks at 284.56, 285.90 and 287.93 eV stand for C–C, C–O and O═C–O consecutively [54,56,57]. The carbon composition in Ma-ZnO NPs further supports the findings in EDX and FTIR.

3.4. In vitro cytotoxicity evaluation of ZnO NPs on Vero cells

3.4.1. MTT assay

The statistics correspond to a dose-dependent cytotoxic effect of ZnO NPs on Vero cells across all time frames in Fig. 13 (a - c). The percentage of cell viability showed a steady drop with increasing doses of C- and Ma-ZnO NPs, indicating that higher concentrations resulted in a lower percentage of cell viability. Comparable findings have been confirmed by other researchers [58–60]. These findings emphasize the need to take consideration on dose dependency when assessing the cytotoxic activity of ZnO NPs on Vero cells.

At 24, 48 and 72 h, the percentage of cell viability upon exposure to 100 μg/mL of C–ZnO NPs were 65.92 %, 60.76 % and 53.67 %, while 100 μg/mL of Ma-ZnO NPs resulted in 75.84 %, 73.64 %, and 63.79 % of cell viability, respectively. The lowest concentration (0.05 μg/mL) of Ma-ZnO NPs did not cause significant cell death as compared to C–ZnO NPs. The present results indicated that the treatment of Ma-ZnO NPs exhibited a higher cell viability compared to C–ZnO NPs treatment However, a significant decrease in cell viability was observed at 72 h, suggesting a more profound cytotoxicity of both the ZnO NPs. This implies that the effects of C- and Ma-ZnO NPs become more pronounced as the exposure duration lengthens. This observation supports the conclusions drawn in previous studies [61,62].

At lower concentrations of Ma-ZnO NPs, specifically between 0.05 and 0.39 μg/mL, the percentage of cell viability exceeds 90 % at 24 h. Similarly, at 48 h, the percentage of cell viability remains above 90 % within the range of 0.05–0.20 μg/mL. On the other hand, when subjected to C–ZnO NPs, only 0.05 μg/mL at 24 h exhibits greater than 90 % cell viability. Therefore, the experiment indicates that the safe concentrations of C- and Ma-ZnO NPs should be lesser than 0.05 and 0.39 μg/mL at 24 h and lower than 0.20 μg/mL for Ma-ZnO NPs at 48 h.

The data showed that C- and Ma-ZnO NPs had a similar pattern of concentration- and time-dependent cytotoxicity on Vero cells which was evidenced by the progressive decline in cell viability percentage. Notably, Ma-ZnO NPs have been found to exhibit lesser cytotoxicity compared to C–ZnO NPs. This reduced cytotoxicity of Ma-ZnO NPs may be attributed to the green synthesis process which
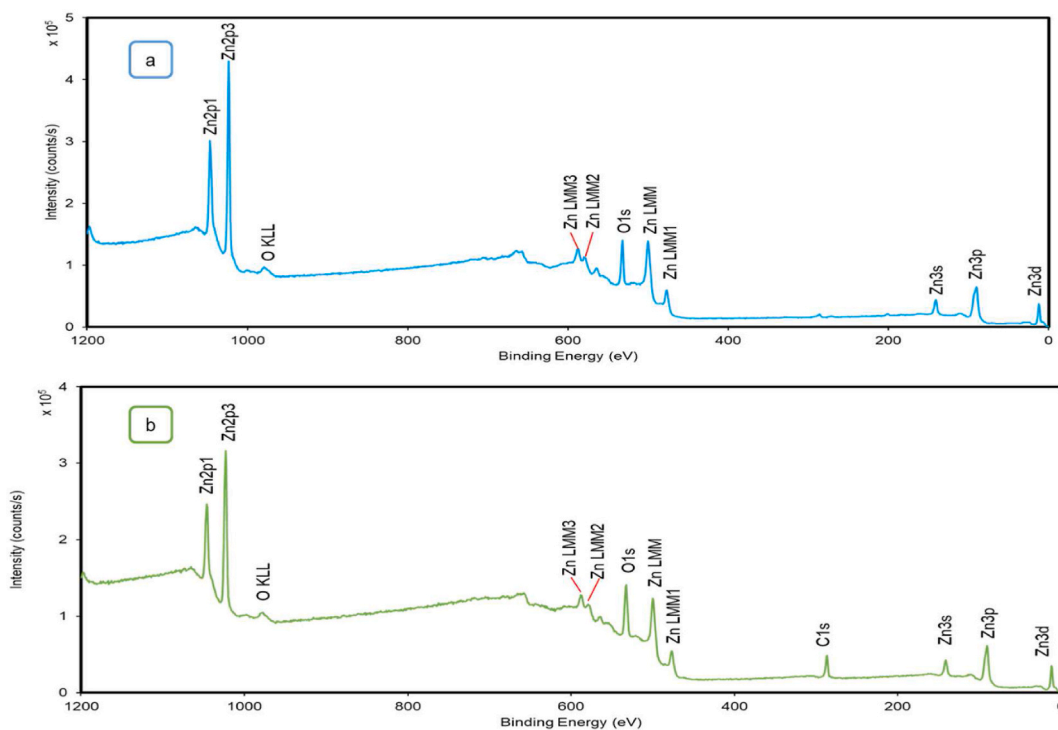

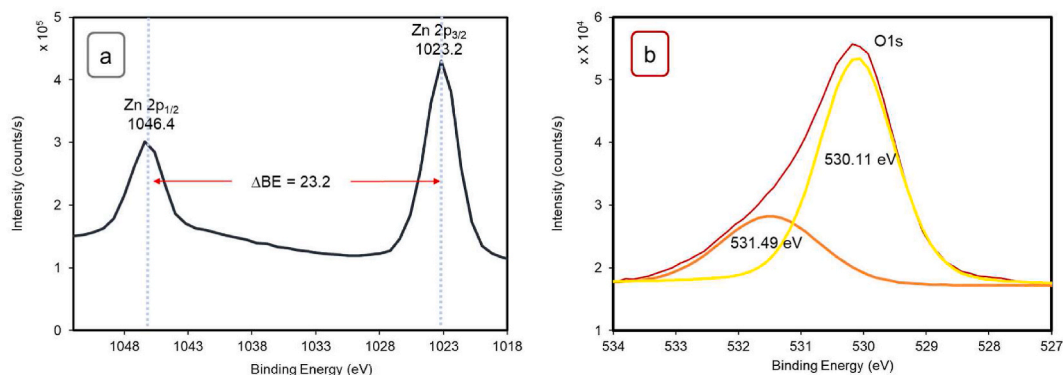**Fig. 10.** XPS spectrum (a) C–ZnO NPs and (b) Ma-ZnO NPs.

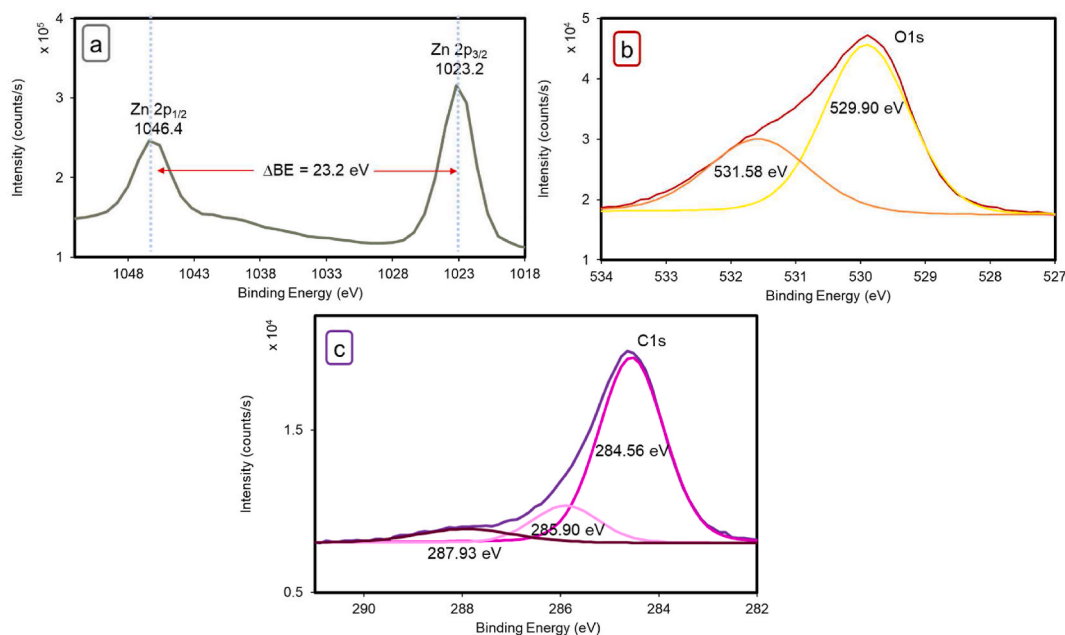**Fig. 11.** XPS spectra of (A) Zn 2p, (B) O 1s in C–ZnO NPs.

Fig. 12. XPS spectra of (A) Zn 2p, (B) O 1s, and (C) C 1s in Ma-ZnO NPs.

involves the use of phytocompounds from *M. acuminata* leaf aqueous extract that allowed better control over the size and surface properties of Ma-ZnO NPs. This control is crucial as the physicochemical characteristics of Ma-ZnO NPs influence their interactions with the cells. The phytocompounds contribute to the formation of smaller-sized, well-dispersed and less-aggregated Ma-ZnO NPs. This ensures the production of NPs with optimized properties that lead to enhanced biocompatibility and reduced cytotoxicity due to its lower surface area than the larger chemically synthesized ZnO NPs.

These findings align with the study conducted by Ref. [63] who compared two types of ZnO NPs with similar spherical shapes but distinct average sizes. Chemical ZnO NPs had a mean size of 27.6 nm and green ZnO NPs, exhibited size of 7.8 nm. The chemical ZnO NPs exhibited higher cytotoxicity compared to the smaller green ZnO NPs. Consistent with El-Waseif's work, this present study demonstrated that larger-sized C–ZnO NPs induce greater cytotoxic effects in contrast to the smaller Ma-ZnO NPs.

The shape of the ZnO NPs additionally plays an essential role in its cytotoxic effects. For instance, in the investigation by Ref. [64], hexagonal shapes and nanorods ZnO NPs were synthesized. Despite having similar size ranges, the nanorods exhibited significantly lower cytotoxicity at 24 h. The synthesis of rod-shaped ZnO NPs in this experiment aligns with previous research which showed lower cytotoxicity as compared to other studies reported in the literature.

A study by Ref. [61] reported similar results where ZnO NPs synthesized through the chemical method exhibited the highest cytotoxicity levels on Vero cells, surpassing those of the green-synthesized ZnO NPs using extracts from *Punica granatum* L. peel and coffee grounds. These findings provide compelling evidence that chemically synthesized ZnO NPs induce greater cytotoxicity compared to green-synthesized ZnO NPs.
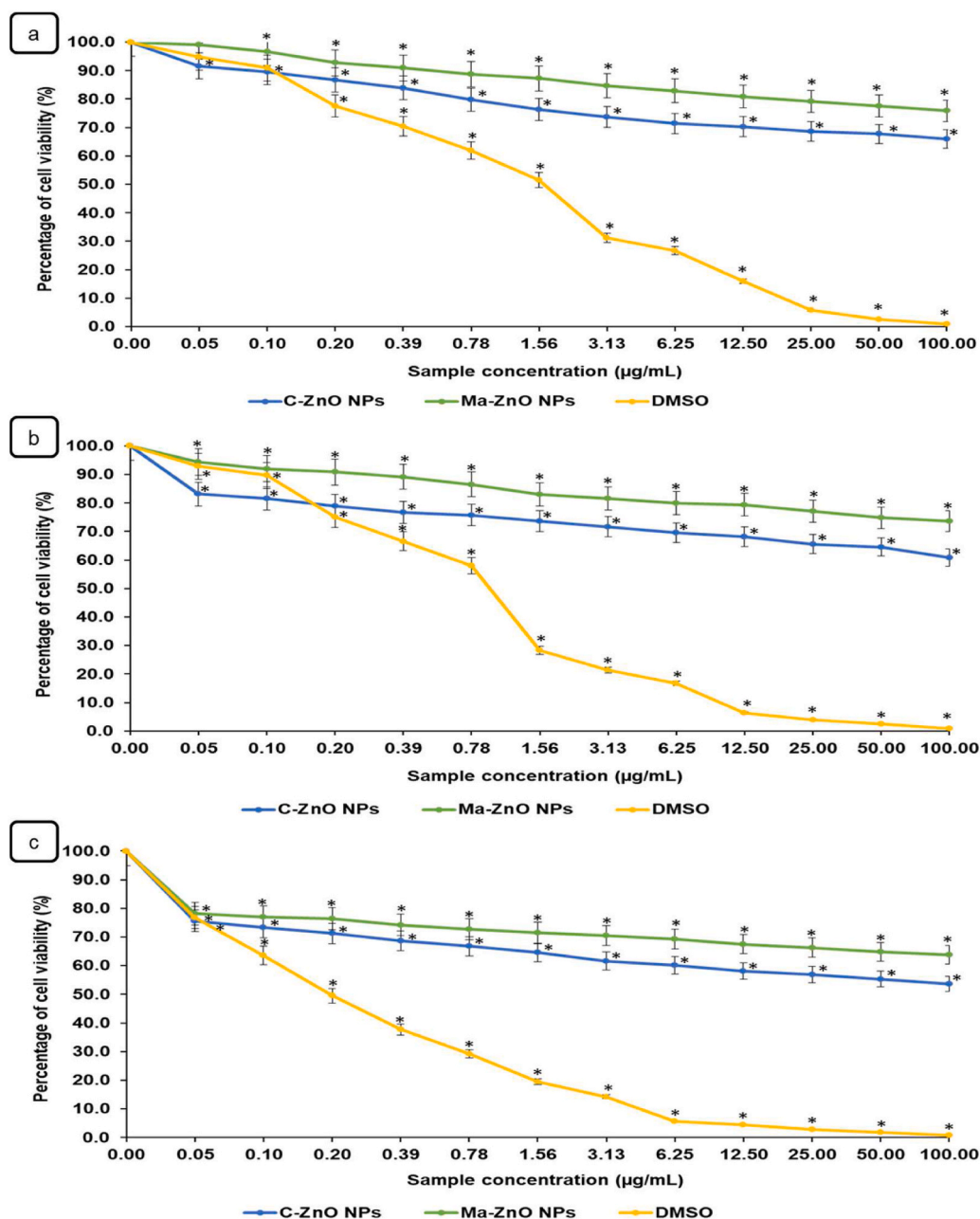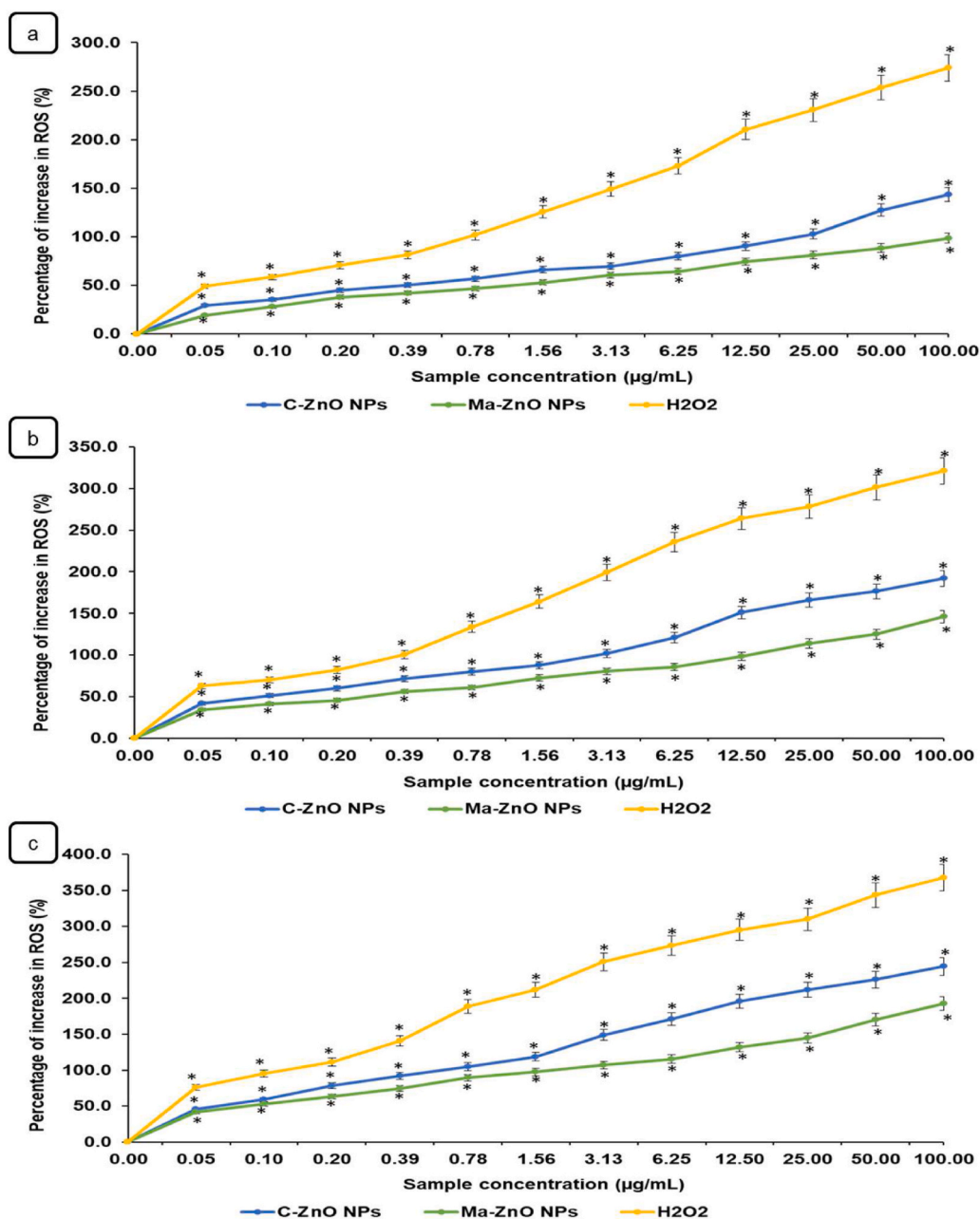
Fig. 13. MTT assay on Vero cells exposed to C- and Ma-ZnO NPs at (a) 24 (b) 48 and (c) 72 h * Indicates the significance difference at $p < 0.05$ between the negative control and ZnO NPs treated Vero cells for each time interval.

3.4.2. ROS assay

2′-7′-dichlorodihydrofluorescein diacetate (DCFH-DA) is an intracellular fluorescent probe that is often employed in cellular studies to access the cell's redox status. DCFH-DA assay was employed to measure ROS levels of C- and Ma-ZnO NPs on Vero cells.

The outcomes of this investigation showed that C- and Ma-ZnO NPs caused an increase in ROS in Vero cells, as shown in Fig. 14 (a – c). The cells exposed to 0.05 µg/mL of C- and Ma-ZnO NPs demonstrated a small increase in ROS generation by 29.31 and 18.95 % at 24 h, respectively. However, 100 µg/mL of C- and Ma-ZnO NPs at 24 h showed a significant escalation in ROS percentage of 143.67 and 98.71, consecutively. The analysis demonstrated a consistent upward trend in the percentage of ROS increase with higher concentrations of both the ZnO NPs across all time intervals. This observation is supported by the notion that several previous studies have reported similar dose-dependent increases in ROS [65–67].

Furthermore, the quantitative analysis also unfolded the duration-dependent increase in the DCF fluorescence intensity. At 24, 48 and 72 h, the percentage of increase in ROS upon exposure to 100 µg/mL of C–ZnO NPs were 143.67 %, 191.85 % and 244.39 %, while

Fig. 14. ROS assay on Vero cells exposed to C- and Ma-ZnO NPs at (a) 24 (b) 48 and (c) 72 h * Indicates the significance difference at $p < 0.05$ between the negative control and ZnO NPs treated Vero cells for each time interval.

100 µg/mL of Ma-ZnO NPs caused an elevation in ROS generation of 98.71 %, 146.03 %, and 192.40 %, respectively. This is evident that the duration of C- and Ma-ZnO NPs exposure plays a major role in the generation of intracellular ROS [68]. showed that ROS production of ZnO NPs was time-dependent; where the fluorescence intensity developed within 6 h and was more pronounced after a 24 h exposure on human bronchial epithelial cells [69]. also concluded that ZnO NPs treatment for 24 h, 48 h and 72 h had ROS generation capability according to the time that is related to the cytotoxic effect on normal skin cells.

Studies into the mechanism of cytotoxic action of ZnO NPs showed that one of the factors contributing to apoptosis in cells treated with ZnO NPs is the production of intracellular ROS. The findings indicate that as ROS levels increase, there is consequential damage to the cell and subsequent cell death. While a moderate level of ROS promotes cell proliferation, elevated levels can lead to oxidative damage of cellular components due to a reduced antioxidant system in the cells [70]. Oxidative stress by the presence of C- and Ma-ZnO NPs, triggers a cascade of detrimental effects within the cells, ultimately leading to impaired functionality and reduced viability as observed in MTT assay. ROS can initiate the oxidation of lipids, proteins, and DNA. These oxidative modifications disrupt

the normal functioning of cellular components, impairing vital cellular processes and triggering cell death pathways. There is a strong correlation between the observed increase in ROS and the subsequent decrease in cell viability. According to Ref. [71], exposure to 20 μg/mL ZnO NPs at 24 h inhibited 73.5 % of mouse embryo fibroblast cell viability and 50 μg/mL of ZnO NPs resulted in a 5-fold elevation in ROS levels compared to the controls which underpin the oxidative stress induced cytotoxicity.

The outcomes of the DCFH-DA assay demonstrate that C- and Ma-ZnO NPs showed a resembling dose- and duration-dependent elevation in intracellular ROS which was proved by the significant rise of ROS production in Vero cells. Noticeably, C–ZnO NPs substantially enhanced intracellular ROS generation as compared to that of Ma-ZnO NPs when measured quantitatively. The ROS production percentage difference of C- and Ma-ZnO NPs exposed cells showed an increase of more than 40 % at 100 μg/mL over all the time frames examined. This shows that C–ZnO NPs induce more oxidative stress in the cells.

The reason behind this observation could be due to the fact that the size difference between C- and Ma-ZnO NPs plays a significant role in the increase in cellular ROS levels. The reduced surface area of Ma-ZnO NPs limits the contact points available for ROS generation, thereby decreasing the overall ROS production compared to the larger and more aggregated C–ZnO NPs. Consequently, the lower levels of ROS generated by Ma-ZnO NPs help to preserve normal cellular functions and minimize oxidative stress-induced cell death thus demonstrating better biocompatibility.
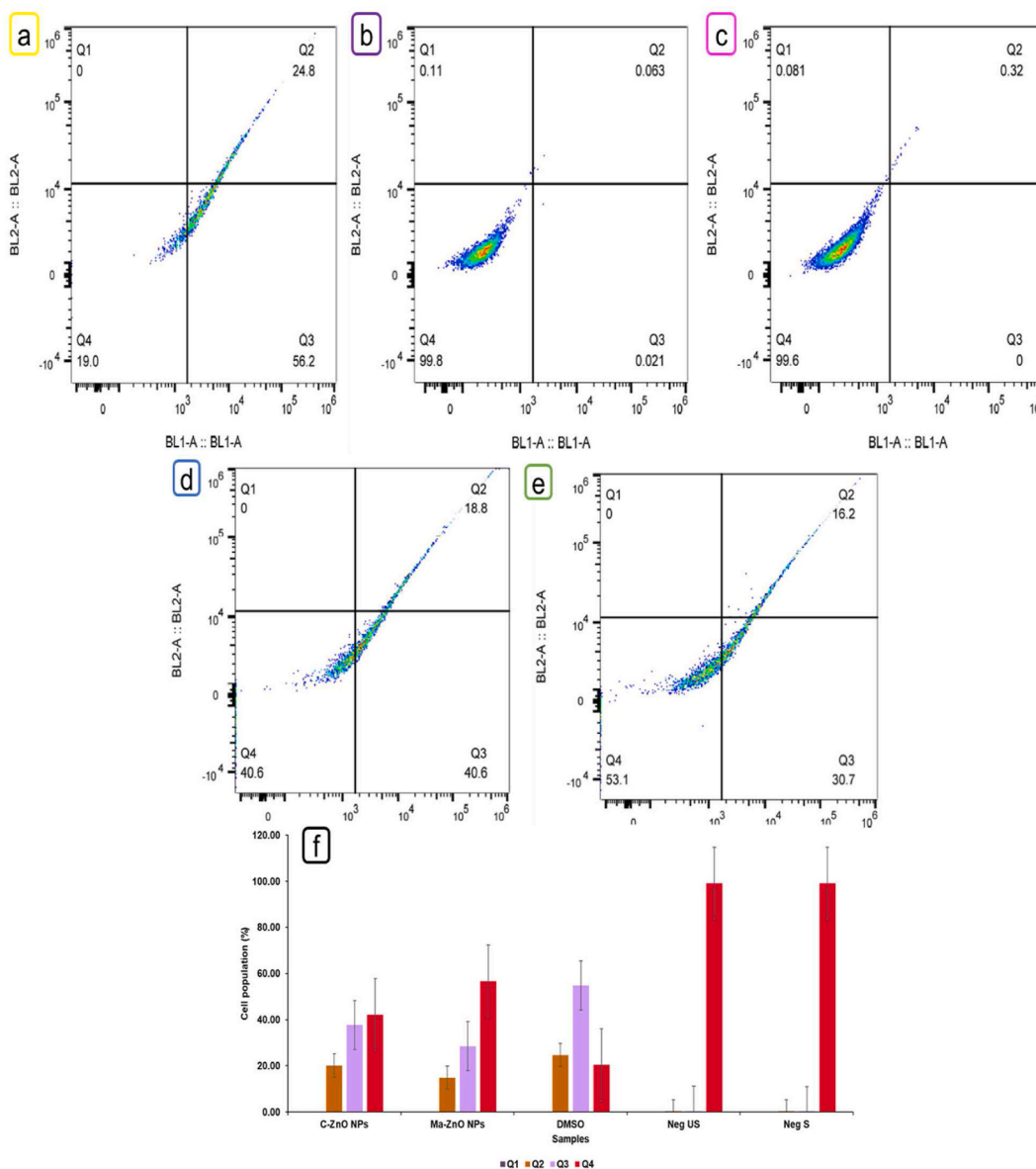
Fig. 15. Flow cytometry analysis of Vero cells' cell viability treated with (a) positive control (DMSO), (b) unstained negative control, (c) stained negative control, (d) 100 μg/mL C–ZnO NPs, (e) 100 μg/mL Ma-ZnO NPs and (f) graph of the cell viability experiment in triplicates at 72 h.

3.4.3. Flow cytometry

Annexin V conjugated with fluorescein isothiocyanate (FITC), when used with 7-AAD (7-Aminoactinomycin D), enabled simultaneous identification and discrimination of viable cells, cells in early or late apoptosis, necrotic or dead cells as well as the cells' DNA content. Flow cytometric analysis provided valuable insights into the dynamics of apoptosis and cell cycle arrest as a consequence to oxidative stress and DNA damage caused by C- and Ma-ZnO NPs [72].

3.4.3.1. Cell viability.

In the positive control (Fig. 15 (a)), a higher number of cells were observed in the second and third quadrants which represent late and early apoptotic cells. This observation strongly suggests that DMSO adversely influenced the apoptosis of Vero cells. Dissimilarity was seen in both the stained and unstained negative controls Fig. 15 (b and c) which displayed more cells in the fourth quadrant, indicative of viable cells, thus confirming the viability of the cells. In addition, the stained negative control effectively demonstrates that the dyes used did not induce any discernible effects on the cells.

In the Ma-ZnO NPs exposed cells (Fig. 15 (d)), a higher proportion of viable cells was observed, along with a reduced percentage of cells in the second and third quadrants, in comparison to the C–ZnO NPs exposed cells (Fig. 15 (e)). These findings indicate that both the ZnO NPs have cytotoxic effects on Vero cells by induction of apoptosis. However, Ma-ZnO NPs induced lesser cytotoxicity when compared to C–ZnO NPs. This result validates the outcomes obtained from the cytotoxicity assay. Fig. 15 (f) illustrates a graph displaying the percentage of cell populations in each quadrant for all the samples in triplicates. The analysis demonstrated that both C- and Ma-ZnO NPs resulted in increased numbers of early apoptotic cells, with just a minor proportion of cells necrosing. These findings collectively indicate that C- and Ma-ZnO NPs primarily triggered the early apoptotic pathway instead of the necrotic.

Comparable findings to this investigation have been observed in multiple research [73]. determined that ZnO NPs from *Sargassum muticum* extract caused a time-dependent increase in late apoptosis in WEHI-3B cells, suggesting an antiproliferative effect through apoptosis. When exposed to Chem ZnO NPs at varying concentrations for 24 h, MCF-7 cells exhibited more number of early apoptotic cells and a small percentage of necrotic cells in a dose-dependent manner (Boroumand Moghaddam et al., 2017) [74]. found that green-synthesized ZnO NPs from *Rubia tinctorum* root extract induced apoptosis in MCF-7 cells after 24 h, with apoptosis levels improving as ZnO-NPs concentration increased. These collective studies indicate the potential apoptotic implications of ZnO NPs in different cells.

3.4.4. Cell cycle

The cell cycle is a series of events that a cell undergoes as it grows and divides into two daughter cells. It consists of distinct phases, including the G1, S, G2, and M phases. Cells in G1 phase have a lower DNA content than cells in S or G2 phase. Similarly, cells in S phase have an intermediate DNA content, while cells in G2 phase have a high DNA content. The fluorescence intensity of cells stained with 7-AAD corresponds to the DNA content, and this information is used to determine the proportions of cells across multiple cell cycle stages.

In the positive control (Fig. 16 (a)), a predominant population of cells was observed in the G1 phase which suggests that oxidative stress-induced DNA damage activates cellular signalling pathways, leading to G1 arrest. Both the stained and unstained negative control cells were found to be evenly distributed across the G1, S, and G2 cell cycle phases, indicating they are undergoing normal cellular functions Fig. 16 (b and c). Notably, a larger quantity of cells was arrested in the G1 phase upon exposure with C–ZnO NPs as compared to Ma-ZnO NPs exposed cells (Fig. 16 (d and e)). This verifies that both the ZnO NPs cause DNA damage that subsequently arrests the cells at the G1 phase. As anticipated, Ma-ZnO NPs induced fewer genetic defects than C–ZnO NPs on Vero cells. This finding aligns with the results obtained from all previous bioassays which demonstrate that Ma-ZnO NPs induce lesser cytotoxicity than C–ZnO NPs. Fig. 16 (f) depicts the percentage of Vero cells across each cell cycle for all the samples in triplicates.

When cells are exposed to ZnO NPs, the elevated levels of ROS result in oxidative stress, that causes damage to the DNA. The DNA damage triggers cellular signalling pathways and induces the G1 phase cell cycle arrest that halts the progression from G1 to S phase. If the damage caused by ROS and ZnO NPs is extensive, the cells undergo apoptosis to eliminate the potentially harmful cells. Furthermore, prolonged G1 arrest may lead to senescence, a state of irreversible growth arrest, which can occur as a response to extensive cellular damage. In summary, exposure to ZnO NPs can induce G1 arrest in cells which is often associated with oxidative stress and DNA damage caused by ROS generation.

Research has proved that ZnO NPs can promote G1 arrest in various cell types, and the findings of other studies align closely with the current investigation. A study reported a significant and dose-dependent increase in the SubG1 phase of the cell cycle in MCF-7 cells exposed to ZnO-NPs from *Rubia tinctorum* root extract [74]. Similarly, a time-dependent increase in the sub-G0/G1 population, representing apoptotic and dead cells, in WEHI-3 cells exposed to ZnO-NPs from *Sargassum muticum* extract was observed [73]. Moreover [75], detected significant alterations in the cell cycle, in SHSY5Y cells, together with mitotic arrest, following 3 and 6 h treatments with chemically synthesized ZnO NPs. These collective findings demonstrate that ZnO NPs can induce cell cycle arrest and apoptosis, reaffirming their cytotoxic effects regardless of the specific phase at which cell arrest occurs.

3.5. Microscopic analysis of ZnO NPs on Vero cells

3.5.1. Inverted microscopy

Microscopic analysis was performed to evaluate the impacts of C- and Ma-ZnO NPs on Vero cells using inverted microscopy at 24, 48, and 72 h to assess the temporal impact of ZnO NPs on cell morphology. Under microscopic observation, the negative control cells displayed an epithelial-like morphology, with an elongated shape. The cell membranes were intact, forming a well-defined boundary
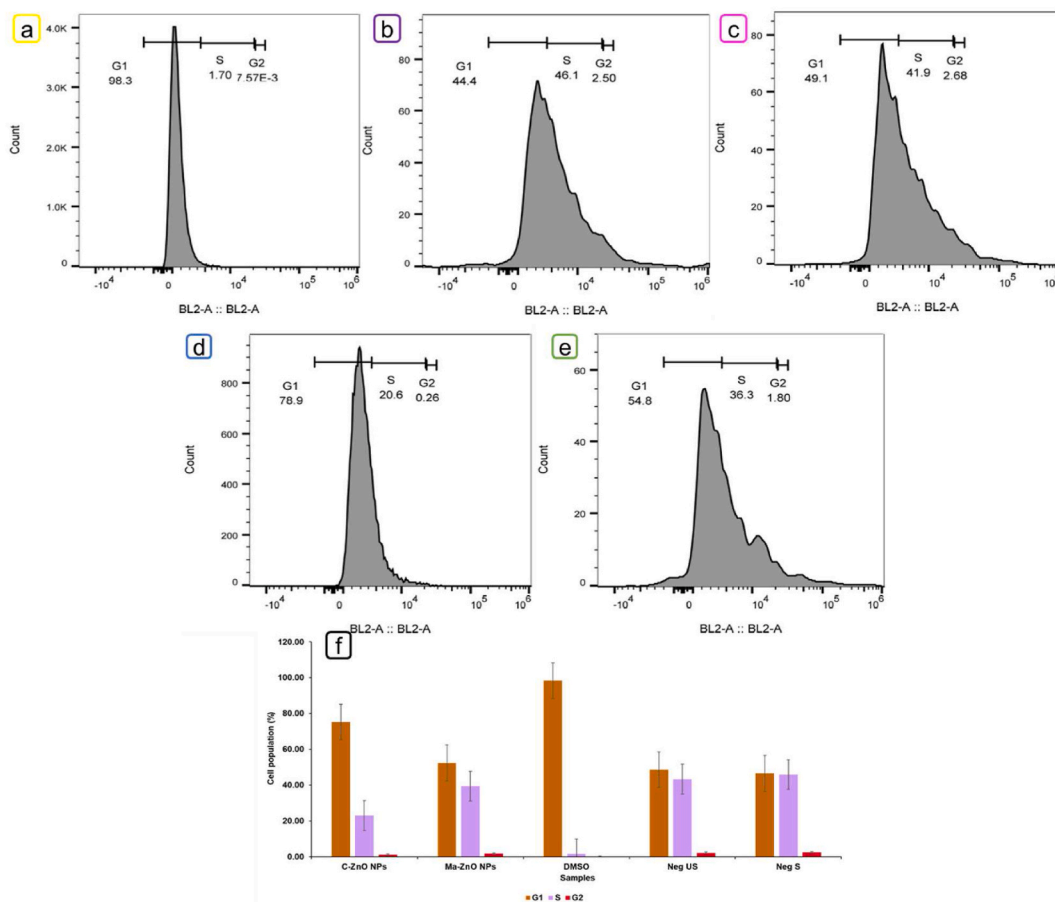
Fig. 16. Flow cytometry analysis of Vero cells' cell cycle treated with (a) positive control (DMSO), (b) Unstained negative control, (c) Stained negative control, (d) 100 μg/mL C–ZnO NPs, (e) 100 μg/mL Ma-ZnO NPs and (f) graph of the cell cycle experiment in triplicates at 72 h.

around each cell as observed in Fig. 17 (a and b). However, at 72 h, a decline in cells was observed in the negative control group (Fig. 17 (c)). This could be due to the depletion of the growth medium over time. In contrast, the positive control cells (Fig. 18 (a – c)) exhibited cell rounding and shrinkage (purple circle). Moreover, these cells detached from the culture flask and formed clusters (yellow circle) as well as fragmented cells with membrane blebbing (red arrow) which is a characteristic feature of apoptotic cells. Additionally, the presence of apoptotic bodies (pink arrow) further confirmed the occurrence of cellular apoptosis.

The cells exposed to C–ZnO NPs exhibited a gradual progression of morphological changes over time. At 24 h, no distinct alteration in cell morphology was observed (Fig. 19 (a)). However, at 48 h, the cells started to exhibit signs of cellular distress as they began to lose their normal shape. Furthermore, the presence of apoptotic bodies was observed suggesting that the C–ZnO NPs exposure triggered apoptotic pathways in the cells (Fig. 19 (b)). At 72 h, the effects of C–ZnO NPs exposure became more pronounced as the cells shrank and detached from the culture flask. Membrane blebbing was also noticed, further indicating cellular damage and disruption
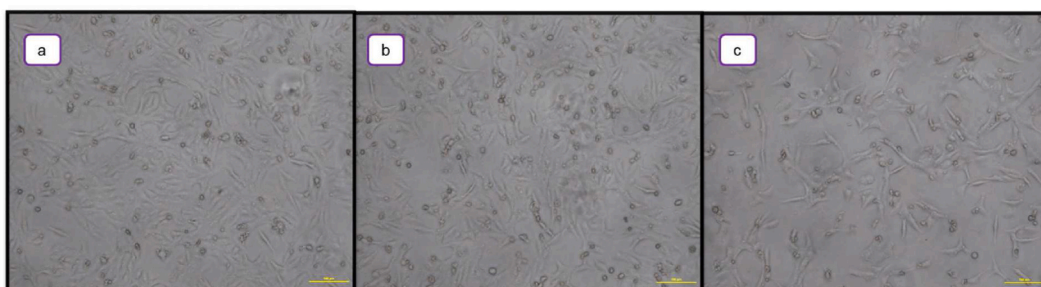
Fig. 17. Inverted microscopy images of Vero cells in the negative control group at (a) 24 h, (b) 48 h, and (c) 72 h.
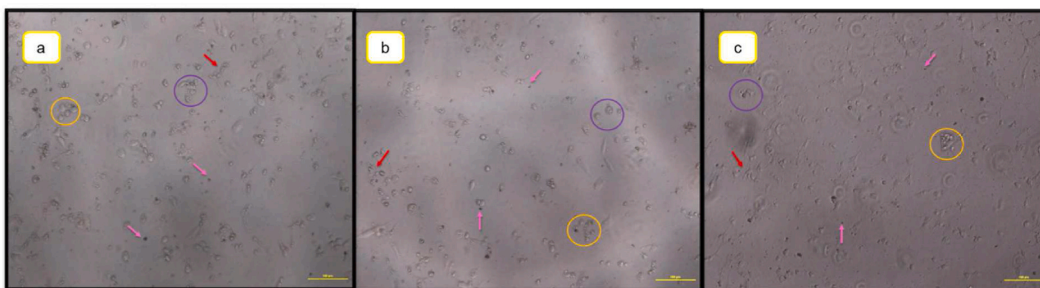
Fig. 18. Inverted microscopy images of Vero cells in the positive control group at (a) 24 h, (b) 48 h, and (c) 72 h.

(Fig. 19 (c)). These cumulative findings demonstrate that the exposure to C–ZnO NPs induced significant morphological changes and apoptotic responses in the cells.

The cells exposed to Ma-ZnO NPs initially appeared healthy and exhibited a normal morphology at both 24 and 48 h, as shown in Fig. 20 (a and b) respectively. However, a minor observation at 48 h showed that a few cells had retracted into a spherical shape, suggesting a slight alteration in cellular structure. It was not until 72 h that more pronounced signs of cellular injury became apparent. At this stage, the Ma-ZnO NPs exposed cells displayed significant cell shrinkage, fragmentation, and the presence of apoptotic bodies (Fig. 20 (c)). These details suggest that the prolonged exposure to Ma-ZnO NPs induced progressive damage to the cells over time, leading to cellular injury and the initiation of apoptotic pathways.

Other studies have also shown that exposure to varying concentrations of ZnO NPs resulted in a gradual loss of their characteristic phenotype, including loss of monolayer, cell rounding and shrinking in comparison to untreated control cells (Fouda et al., 2018; Majeed et al., 2019). A431 cells treated with ZnO NPs displayed characteristic apoptotic changes, while A549 cells exposed to ZnO NPs showed a round morphology with nuclear condensation [76,77].
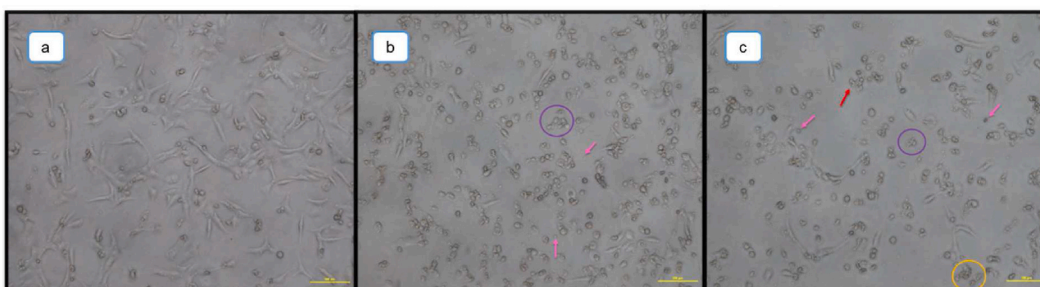
3.5.2. Fluorescence microscopy

Fluorescence microscopy imaging of the DCFH-DA assay provided a valuable tool for qualitatively visualizing intracellular ROS levels in Vero cells upon exposure to C- and Ma-ZnO NPs. According to Fig. 21 (a and b), the negative control cells at both 24 and 48 h displayed baseline levels of ROS with minimal fluorescence intensity. However, a slight elevation in fluorescence was observed at 72 h, which could due be to the stress induced by the depletion of the growth medium (as depicted in Fig. 21 (c)). Conversely, the positive control groups exhibited a notable increase in the level of ROS as indicated by the intense cytosolic green fluorescence intensity (as illustrated in Fig. 22 (a). Moreover, the morphological changes in these cells became evident at 48 h, characterized by a loss of their normal morphology. At 72 h, the cells exhibited rounding and shrinking as depicted in Fig. 22 (b and c).

Cells treated with C–ZnO NPs exhibited a small increment in ROS generation at 24 h (Fig. 23 (a)). At 48 h, a slightly higher level of ROS signals became evident; however, the cells still maintained their characteristic healthy epithelial shape (Fig. 23 (b)). Interestingly, at 72 h, a substantial elevation in ROS formation was noticed in cells exposed to C–ZnO NPs with the normal cellular morphology loss and the presence of some cellular deformation, as depicted in Fig. 23 (c). These findings suggest that prolonged exposure to C–ZnO NPs induces a progressive rise in ROS production, thereby indicating the cytotoxic effects of C–ZnO NPs.

Analogously, the cells treated with Ma-ZnO NPs revealed a similar pattern. At 24 h (Fig. 24 (a)), minimal ROS production was observed. However, at 48 h, a noticeable increase in green fluorescence, indicating elevated ROS levels (Fig. 24 (b). The trend continued at 72 h, with the highest intensity of fluorescence seen in Fig. 24 (c). Additionally, the cells exposed to Ma-ZnO NPs exhibited irregularly shaped cell membranes and had lost their characteristic morphology. These observations highlight that prolonged exposure to Ma-ZnO NPs induces a gradual elevation in ROS production that can cause cellular damage.

These findings indicate that both C- and Ma-ZnO NPs exhibit similar time-dependent increases in ROS levels, with C–ZnO NPs demonstrating a slightly higher elevation in fluorescence intensity compared to Ma-ZnO NPs. This observation aligns with the

Fig. 19. Inverted microscopy images of Vero cells exposed to 100 µg/mL of C–ZnO NPs at (a) 24 h, (b) 48 h, and (c) 72 h.

Fig. 20. Inverted microscopy images of Vero cells exposed to 100 μg/mL of Ma-ZnO NPs at (a) 24 h, (b) 48 h, and (c) 72 h.
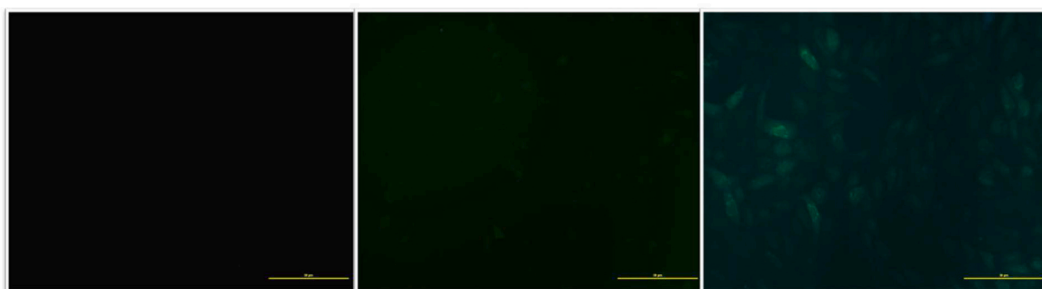

Fig. 21. Fluorescence microscopy images of Vero cells in the negative control group at (a) 24 h, (b) 48 h, and (c) 72 h.
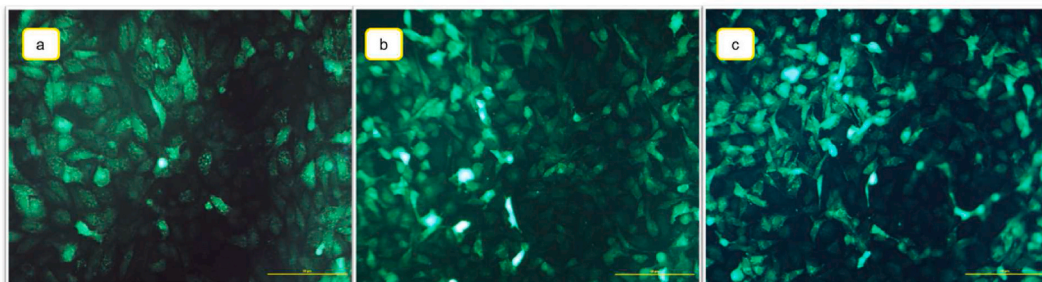

Fig. 22. Fluorescence microscopy images of Vero cells in the positive control group at (a) 24 h, (b) 48 h, and (c) 72 h.

Fig. 23. Fluorescence microscopy images of Vero cells exposed to 100 μg/mL of C–ZnO NPs at (a) 24 h, (b) 48 h, and (c) 72 h.

quantitative data presented earlier. In support of these findings, a study by Ref. [78] demonstrated an increase in ROS levels in HepG2 cells following 6 h subjection to ZnO NPs. Furthermore [69], illustrated a gradual increase in green fluorescence intensity in ZnO NPs-treated normal skin cells over different culture times of 24, 48, and 72 h. These references highlight the consistent impact of ZnO NPs on cellular oxidative stress over prolonged durations.
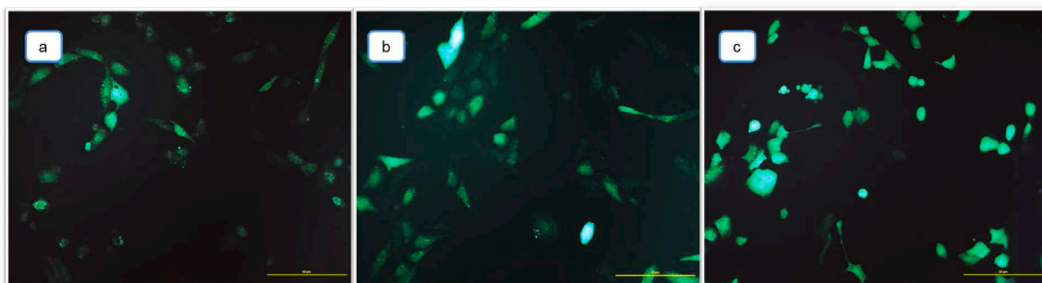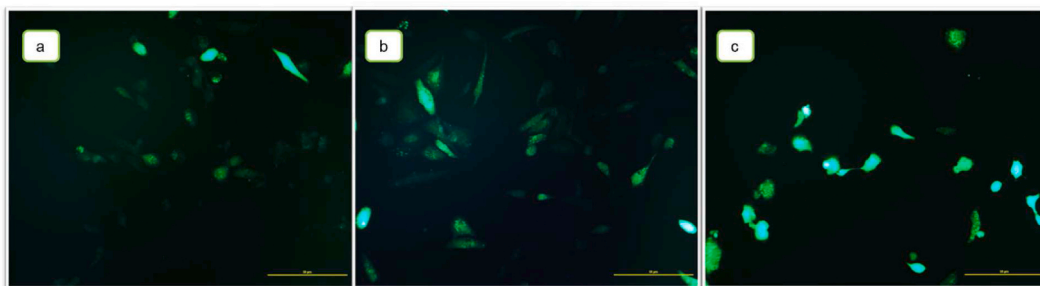
Fig. 24. Fluorescence microscopy images of Vero cells exposed to 100 μg/mL of Ma-ZnO NPs at (a) 24 h, (b) 48 h, and (c) 72 h.

4. Conclusion

The cytotoxicity studies reveal that C–ZnO NPs and Ma-ZnO NPs exhibit dose- and time-dependent effects on Vero cell viability. The safe concentrations (more than 90 % cell viability) of C- and Ma-ZnO NPs are lesser than 0.05 and 0.39 μg/mL at 24 h and lower than 0.20 μg/mL in the case of Ma-ZnO NPs at 48 h. Furthermore, the mechanism of Vero cell death indicated that both C–ZnO NPs and Ma-ZnO NPs induced early apoptotic pathways. Additionally, the lesser DNA damage noted in Vero cells treated with Ma-ZnO NPs supports the notion that green synthesized ZnO NPs are less harmful to normal cells. It is evident that both C–ZnO NPs as well as Ma-ZnO NPs exert cytotoxic effects on normal cells through ROS production, direct interactions with the cells, and the induction of apoptosis. However, the relatively lower adverse effects of Ma-ZnO NPs compared to C–ZnO NPs make them a more suitable choice for incorporation into everyday products. By promoting the utilization of green synthesized ZnO NPs, we can move closer to achieving sustainable development objectives while minimizing the impact on human health and the environment.

Declaration

Review and/or approval by an ethics committee is not applicable for this study since no human or animal subjects were involved, and all materials were sourced from a reputable provider adhering to ethical guidelines.

Data availability statement

The data used to support the findings of this study are included within the article.

CRediT authorship contribution statement

Harshyini Maheswaran: Writing – original draft, Methodology, Investigation, Data curation. **Sinouvassane Djearamane:** Writing – review & editing, Supervision, Methodology, Funding acquisition. **Anto Cordelia Tanislaus Antony Dhanapal:** Writing – review & editing, Supervision, Methodology. **Ling Shing Wong:** Writing – review & editing, Supervision.

Declaration of competing interest

The authors declare that they have no known competing financial interests or personal relationships that could have appeared to influence the work reported in this paper.

References

[1] C. Anandharamakrishnan, S. Parthasarathi, Food Nanotechnology: Principles and Applications, Taylor & Francis Group, 2019.
[2] S.K. Prasad, Modern Concepts in Nanotechnology, Discovery, Publishing House, 2008.
[3] A. Moezzi, A.M. McDonagh, M.B. Cortie, Zinc oxide particles: synthesis, properties and applications, Chem. Eng. J. 185–186 (2012) 1–22, https://doi.org/10.1016/j.cej.2012.01.076.

[4] S. Djearamane, L.S. Wong, Y.M. Lim, P.F. Lee, Cytotoxic effects of zinc oxide nanoparticles on Chlorella Vulgaris. http://eprints.utar.edu.my/4140/, 2019. (Accessed 16 March 2022).

[5] A. Kołodziejczak-Radzimska, T. Jesionowski, Zinc oxide—from synthesis to application: a review, Materials 7 (2014) 2833–2881, https://doi.org/10.3390/ma7042833.

[6] H. Maheswaran, L.S. Wong, A.C.T.A. Dhanapal, R.T. Narendhirakannan, A.K. Janakiraman, S. Djearamane, Toxicity of zinc oxide nanoparticles on human skin Dermal cells, Journal of Experimental Biology and Agricultural Sciences 9 (2021) S95–S100, https://doi.org/10.18006/2021.9(Spl-1-GCSGD_2020).S95.S100.

[7] P. Kaur, R. Thakur, S. Kumar, N. Dilbaghi, Interaction of ZnO nanoparticles with food borne pathogens Escherichia coli DH5α and Staphylococcus aureus 5021 & their bactericidal efficacy, AIP Conf. Proc. 1393 (2011) 153–154, https://doi.org/10.1063/1.3653655.

[8] P. Narayanan, S. Wilson, A. Abraham, M. Sevanan, Synthesis, characterization, and antimicrobial activity of zinc oxide nanoparticles against human pathogens, BioNanoScience 2 (2012), https://doi.org/10.1007/s12668-012-0061-6.

[9] T.N.V.K.V. Prasad, P. Sudhakar, Y. Sreenivasulu, P. Latha, V. Munaswamy, K. Reddy, S. Sreenivasan, P. Panikkanvalappil, P. Thalappil, Effect of nanoscale zinc oxide particles on the germination, growth and yield of peanut, J. Plant Nutr. 35 (2012) 905–927, https://doi.org/10.1080/01904167.2012.663443.

[10] H. Mirzaei, M. Darroudi, Zinc oxide nanoparticles: biological synthesis and biomedical applications, Ceram. Int. 43 (2017) 907–914, https://doi.org/10.1016/j.ceramint.2016.10.051.

[11] M.J. Akhtar, M. Ahamed, S. Kumar, M.M. Khan, J. Ahmad, S.A. Alrokayan, Zinc oxide nanoparticles selectively induce apoptosis in human cancer cells through reactive oxygen species, Int. J. Nanomed. 7 (2012) 845–857, https://doi.org/10.2147/IJN.S29129.

[12] C. Hanley, J. Layne, A. Punnoose, K.M. Reddy, I. Coombs, A. Coombs, K. Feris, D. Wingett, Preferential killing of cancer cells and activated human T cells using ZnO nanoparticles, Nanotechnology 19 (2008) 295103, https://doi.org/10.1088/0957-4484/19/29/295103.

[13] H. Agarwal, S. Venkat Kumar, S. Rajeshkumar, A review on green synthesis of zinc oxide nanoparticles – an eco-friendly approach, Resource-Efficient Technologies 3 (2017) 406–413, https://doi.org/10.1016/j.reffit.2017.03.002.

[14] S. Karakuş, Sonochemical Reactions, BoD – Books on Demand, 2020.

[15] V. Prakash, R. Henry, A.K. Patel, J. Pawar, Synthesize and characterization of zinc oxide nanomaterial specifically for sensor development, in: 2018 2nd International Conference on Electronics, Materials Engineering & Nano-Technology (IEMENTech), IEEE, Kolkata, 2018, pp. 1–4, https://doi.org/10.1109/IEMENTECH.2018.8465165.

[16] Y.A.Mohd Esa, N. Sapawe, A short review on zinc metal nanoparticles synthesize by green chemistry via natural plant extracts, Mater. Today: Proc. 31 (2020) 386–393, https://doi.org/10.1016/j.matpr.2020.07.184.

[17] M.K.H. Mohd Nazri, N. Sapawe, A short review on plants extract mediated synthesis of copper oxide nanoparticles, Mater. Today: Proc. 31 (2020) A38–A41, https://doi.org/10.1016/j.matpr.2020.10.966.

[18] D.R. Jones, Handbook of Diseases of Banana, Abaca and Enset, CABI, 2018.

[19] ProMusa, Banana-producing countries portal, ProMusa is a project to improve the understanding of banana and to inform discussions on this atypical crop. http://www.promusa.org/Banana-producing+countries+portal, 2018. (Accessed 16 February 2021).

[20] S. Elanthikkal, U. Gopalakrishnapanicker, S. Varghese, J.T. Guthrie, Cellulose microfibres produced from banana plant wastes: isolation and characterization, Carbohydrate Polymers 80 (2010) 852–859, https://doi.org/10.1016/j.carbpol.2009.12.043.

[21] O.B. Ezeudu, J.C. Agunwamba, T.S. Ezeudu, U.C. Ugochukwu, I.C. Ezeasor, Natural leaf-type as food packaging material for traditional food in Nigeria: sustainability aspects and theoretical circular economy solutions, Environ. Sci. Pollut. Res. 28 (2020) 8833–8843, https://doi.org/10.1007/s11356-020-11268-z.

[22] T.G. Smijs, S. Pavel, Titanium dioxide and zinc oxide nanoparticles in sunscreens: focus on their safety and effectiveness, Nanotechnol. Sci. Appl. 4 (2011) 95–112, https://doi.org/10.2147/NSA.S19419.

[23] Z. Chen, R. Bertin, G. Froldi, EC50 estimation of antioxidant activity in DPPH assay using several statistical programs, Food Chem. 138 (2013) 414–420, https://doi.org/10.1016/j.foodchem.2012.11.001.

[24] E.J. Garcia, T.L.C. Oldoni, S.M. de Alencar, A. Reis, A.D. Loguercio, R.H.M. Grande, Antioxidant activity by DPPH assay of potential solutions to be applied on bleached teeth, Braz. Dent. J. 23 (2012) 22–27, https://doi.org/10.1590/S0103-64402012000100004.

[25] S.B. Kedare, R.P. Singh, Genesis and development of DPPH method of antioxidant assay, J. Food Sci. Technol. 48 (2011) 412–422, https://doi.org/10.1007/s13197-011-0251-1.

[26] M. Naseer, U. Aslam, B. Khalid, B. Chen, Green route to synthesize Zinc Oxide Nanoparticles using leaf extracts of Cassia fistula and Melia azadarach and their antibacterial potential, Sci. Rep. 10 (2020) 9055, https://doi.org/10.1038/s41598-020-65949-3.

[27] T. Varadavenkatesan, E. Lyubchik, S. Pai, A. Pugazhendhi, R. Vinayagam, R. Selvaraj, Photocatalytic degradation of Rhodamine B by zinc oxide nanoparticles synthesized using the leaf extract of Cyanometra ramiflora, J. Photochem. Photobiol. B Biol. 199 (2019) 111621, https://doi.org/10.1016/j.jphotobiol.2019.111621.

[28] A. Król, P. Pomastowski, K. Rafińska, V. Railean-Plugaru, B. Buszewski, Zinc oxide nanoparticles: synthesis, antiseptic activity and toxicity mechanism, Adv. Colloid Interface Sci. 249 (2017) 37–52, https://doi.org/10.1016/j.cis.2017.07.033.

[29] A.A. Barzinjy, H.H. Azeez, Green synthesis and characterization of zinc oxide nanoparticles using Eucalyptus globulus Labill. leaf extract and zinc nitrate hexahydrate salt, SN Appl. Sci. 2 (2020) 991, https://doi.org/10.1007/s42452-020-2813-1.

[30] E.E. Imade, T.O. Ajiboye, A.E. Fadiji, D.C. Onwudiwe, O.O. Babalola, Green synthesis of zinc oxide nanoparticles using plantain peel extracts and the evaluation of their antibacterial activity, Scientific African 16 (2022) e01152, https://doi.org/10.1016/j.sciaf.2022.e01152.

[31] J. Jiang, J. Pi, J. Cai, The advancing of zinc oxide nanoparticles for biomedical applications, Bioinorgan. Chem. Appl. 2018 (2018) e1062562, https://doi.org/10.1155/2018/1062562.

[32] K.L. Foo, U. Hashim, K. Muhammad, C.H. Voon, Sol–gel synthesized zinc oxide nanorods and their structural and optical investigation for optoelectronic application, Nanoscale Res. Lett. 9 (2014) 429, https://doi.org/10.1186/1556-276X-9-429.

[33] H.M.H. Al-Kordy, S.A. Sabry, M.E.M. Mabrouk, Statistical optimization of experimental parameters for extracellular synthesis of zinc oxide nanoparticles by a novel haloalaliphilic Alkalibacillus sp.W7, Sci. Rep. 11 (2021) 10924, https://doi.org/10.1038/s41598-021-90408-y.

[34] S.K. Chaudhuri, L. Malodia, Biosynthesis of zinc oxide nanoparticles using leaf extract of Calotropis gigantea: characterization and its evaluation on tree seedling growth in nursery stage, Appl. Nanosci. 7 (2017) 501–512, https://doi.org/10.1007/s13204-017-0586-7.

[35] D. Gnanasangeetha, D. SaralaThambavani, One pot synthesis of zinc oxide nanoparticles via chemical and green method, Res. J. Material Sci. 1 (2013) 1–8.

[36] S.S. Kumar, P. Venkateswarlu, V.R. Rao, G.N. Rao, Synthesis, characterization and optical properties of zinc oxide nanoparticles, Int. Nano Lett. 3 (2013) 30, https://doi.org/10.1186/2228-5326-3-30.

[37] S. Mustapha, M.M. Ndamitso, A.S. Abdulkareem, J.O. Tijani, D.T. Shuaib, A.K. Mohammed, A. Sumaila, Comparative study of crystallite size using Williamson-Hall and Debye-Scherrer plots for ZnO nanoparticles, Adv. Nat. Sci. Nanosci. Nanotechnol. 10 (2019) 045013, https://doi.org/10.1088/2043-6254/ab52f7.

[38] S.N. Botewad, V.G. Pahurkar, G.G. Muley, D.K. Gaikwad, G.A. Bodkhe, M.D. Shirsat, P.P. Pawar, PANI-ZnO cladding-modified optical fiber biosensor for urea sensing based on evanescent wave absorption, Frontiers in Materials 7 (2020). https://www.frontiersin.org/articles/10.3389/fmats.2020.00184. (Accessed 15 January 2023).

[39] Y.R. Somarathne, H. Samarasinghe, S. Siriwadena, D. Silva, D.V. Mallikarachchi, Effect of nanoZnO over conventional ZnO on preservation of concentrated natural rubber latex, Journal of the Rubber Research Institute of Sri Lanka 98 (2018) 65–79, https://doi.org/10.4038/jrrisl.v98i0.1876.

[40] S. Mahalakshmi, N. Hema, P.P. Vijaya, In vitro biocompatibility and antimicrobial activities of zinc oxide nanoparticles (ZnO NPs) prepared by chemical and green synthetic route— a comparative study, BioNanoSci 10 (2020) 112–121, https://doi.org/10.1007/s12668-019-00698-w.

[41] P. Jamdagni, P. Khatri, J.S. Rana, Green synthesis of zinc oxide nanoparticles using flower extract of Nyctanthes arbor-tristis and their antifungal activity, J. King Saud Univ. Sci. 30 (2018) 168–175, https://doi.org/10.1016/j.jksus.2016.10.002.

[42] S. Vijayakumar, S. Mahadevan, P. Arulmozhi, S. Sriram, P.K. Praseetha, Green synthesis of zinc oxide nanoparticles using Atalantia monophylla leaf extracts: characterization and antimicrobial analysis, Mater. Sci. Semicond. Process. 82 (2018) 39–45, https://doi.org/10.1016/j.mssp.2018.03.017.

[43] S. Fakhari, M. Jamzad, H. Kabiri Fard, Green synthesis of zinc oxide nanoparticles: a comparison, Green Chem. Lett. Rev. 12 (2019) 19–24, https://doi.org/10.1080/17518253.2018.1547925.

[44] N. Jayarambabu, Germination and growth characteristics of mungbean seeds (vigna radiata L.) affected by synthesized zinc oxide nanoparticles, International Journal of Current Engineering and Technology 4 (2014) 5.

[45] F.M. Mohammadi, N. Ghasemi, Influence of temperature and concentration on biosynthesis and characterization of zinc oxide nanoparticles using cherry extract, J Nanostruct Chem 8 (2018) 93–102, https://doi.org/10.1007/s40097-018-0257-6.

[46] A.M. Pillai, V.S. Sivasankarapillai, A. Rahdar, J. Joseph, F. Sadeghfar, R. Anuf A, K. Rajesh, G.Z. Kyzas, Green synthesis and characterization of zinc oxide nanoparticles with antibacterial and antifungal activity, J. Mol. Struct. 1211 (2020) 128107, https://doi.org/10.1016/j.molstruc.2020.128107.

[47] O. Kalu, J.A. Duarte Moller, A. Reyes Rojas, Structural and optical properties of cadmium magnesium zinc oxide (CdMgZnO) nanoparticles synthesized by sol–gel method, Phys. Lett. 383 (2019) 1037–1046, https://doi.org/10.1016/j.physleta.2018.11.052.

[48] S.P. Rajendran, K. Sengodan, Synthesis and characterization of zinc oxide and iron oxide nanoparticles using *Sesbania grandiflora* leaf extract as reducing agent, Journal of Nanoscience 2017 (2017) e8348507, https://doi.org/10.1155/2017/8348507.

[[49] N.S. Ferreira, J.M. Sasaki, R.S. Silva, J.M. Attah-Baah, M.A. Macêdo, Visible-light-responsive photocatalytic activity significantly enhanced by active [$V_{Zn} + V_O^+$] defects in self-assembled ZnO nanoparticles, Inorg. Chem. 60 (2021) 4475–4496, https://doi.org/10.1021/acs.inorgchem.0c03327.

[50] J. Lv, Z. Yang, C. Wang, S. Wang, Y. Ma, G. Zhou, J. Jiang, Q. Zhu, M. Zhao, X. Chen, Effect of vacuum annealing on solar light response and photocatalytic performance of Ag nanoparticle-modified ZnO thin films, Appl. Phys. A 126 (2020) 290, https://doi.org/10.1007/s00339-020-3460-5.

[51] J. de O. Primo, C. Bittencourt, S. Acosta, A. Sierra-Castillo, J.-F. Colomer, S. Jaerger, V.C. Teixeira, F.J. Anaissi, Synthesis of zinc oxide nanoparticles by ecofriendly routes: adsorbent for copper removal from wastewater, Front. Chem. 8 (2020). https://www.frontiersin.org/articles/10.3389/fchem.2020.571790. (Accessed 28 January 2023).

[52] K. Rambabu, G. Bharath, F. Banat, P.L. Show, Green synthesis of zinc oxide nanoparticles using Phoenix dactylifera waste as bioreductant for effective dye degradation and antibacterial performance in wastewater treatment, J. Hazard Mater. 402 (2021) 123560, https://doi.org/10.1016/j.jhazmat.2020.123560.

[53] M. Claros, M. Setka, Y.P. Jimenez, S. Vallejos, AACVD synthesis and characterization of iron and copper oxides modified ZnO structured films, Nanomaterials 10 (2020) 471, https://doi.org/10.3390/nano10030471.

[54] E.F. El-Belely, M.M.S. Farag, H.A. Said, A.S. Amin, E. Azab, A.A. Gobouri, A. Fouda, Green synthesis of zinc oxide nanoparticles (ZnO-NPs) using arthrospira platensis (class: cyanophyceae) and evaluation of their biomedical activities, Nanomaterials 11 (2021) 95, https://doi.org/10.3390/nano11010095.

[55] C. Wang, H. Fan, X. Ren, J. Fang, Room temperature synthesis and enhanced photocatalytic property of CeO2/ZnO heterostructures, Appl. Phys. A 124 (2018) 99, https://doi.org/10.1007/s00339-017-1543-8.

[56] G. Jnido, G. Ohms, W. Viöl, Deposition of zinc oxide coatings on wood surfaces using the solution precursor plasma spraying process, Coatings 11 (2021) 183, https://doi.org/10.3390/coatings11020183.

[57] B. Sivaranjini, M. Rajkumar, C. Ganesh, S. Umadevi, Vertical alignment of liquid crystals over a functionalized flexible substrate, Sci. Rep. 8 (2018), https://doi.org/10.1038/s41598-018-27039-3.

[58] A. Fouda, S. EL-Din Hassan, S.S. Salem, T.I. Shaheen, In-Vitro cytotoxicity, antibacterial, and UV protection properties of the biosynthesized Zinc oxide nanoparticles for medical textile applications, Microb. Pathog. 125 (2018) 252–261, https://doi.org/10.1016/j.micpath.2018.09.030.

[59] S. Majeed, M. Danish, M.H.B. Ismail, M.T. Ansari, M.N.M. Ibrahim, Anticancer and apoptotic activity of biologically synthesized zinc oxide nanoparticles against human colon cancer HCT-116 cell line- in vitro study, Sustainable Chemistry and Pharmacy 14 (2019) 100179, https://doi.org/10.1016/j.scp.2019.100179.

[60] H. Mohd Yusof, N. Abdul Rahman, R. Mohamad, U.H. Zaidan, A.A. Samsudin, Biosynthesis of zinc oxide nanoparticles by cell-biomass and supernatant of Lactobacillus plantarum TA4 and its antibacterial and biocompatibility properties, Sci. Rep. 10 (2020) 19996, https://doi.org/10.1038/s41598-020-76402-w.

[61] H.M. Abdelmigid, N.A. Hussien, A.A. Alyamani, M.M. Morsi, N.M. AlSufyani, H.A. Kadi, Green synthesis of zinc oxide nanoparticles using pomegranate fruit peel and solid coffee grounds vs. Chemical method of synthesis, with their biocompatibility and antibacterial properties investigation, Molecules 27 (2022) 1236, https://doi.org/10.3390/molecules27041236.

[62] S. S., V. K., P. S., R. N., K. K., In vitro cytotoxicity of zinc oxide, iron oxide and copper nanopowders prepared by green synthesis, Toxicol Rep 4 (2017) 427–430, https://doi.org/10.1016/j.toxrep.2017.07.005.

[63] El-Waseif, Cytotoxicity and antimicrobial activity of naturally and chemically synthesized zinc oxide nanoparticles, Journal of The Arab Society for Medical Research 14 (2019) 42.51, https://doi.org/10.4103/jasmr.jasmr_8_19.

[64] A.A. Mohamed, A. Fouda, M.A. Abdel-Rahman, S.E.-D. Hassan, M.S. El-Gamal, S.S. Salem, T.I. Shaheen, Fungal strain impacts the shape, bioactivity and multifunctional properties of green synthesized zinc oxide nanoparticles, Biocatal. Agric. Biotechnol. 19 (2019) 101103, https://doi.org/10.1016/j.bcab.2019.101103.

[65] P. Patel, K. Kansara, V.A. Senapati, R. Shanker, A. Dhawan, A. Kumar, Cell cycle dependent cellular uptake of zinc oxide nanoparticles in human epidermal cells, Mutagenesis 31 (2016) 481–490, https://doi.org/10.1093/mutage/gew014.

[66] V. Sharma, R.K. Shukla, N. Saxena, D. Parmar, M. Das, A. Dhawan, DNA damaging potential of zinc oxide nanoparticles in human epidermal cells, Toxicol. Lett. 185 (2009) 211–218, https://doi.org/10.1016/j.toxlet.2009.01.008.

[67] D. Vergara-Llanos, T. Koning, M.F. Pavicic, H. Bello-Toledo, A. Díaz-Gómez, A. Jaramillo, M. Melendrez-Castro, P. Ehrenfeld, G. Sánchez-Sanhueza, Antibacterial and cytotoxic evaluation of copper and zinc oxide nanoparticles as a potential disinfectant material of connections in implant provisional abutments: an in-vitro study, Arch. Oral Biol. 122 (2021) 105031, https://doi.org/10.1016/j.archoralbio.2020.105031.

[68] C.-C. Huang, R.S. Aronstam, D.-R. Chen, Y.-W. Huang, Oxidative stress, calcium homeostasis, and altered gene expression in human lung epithelial cells exposed to ZnO nanoparticles, Toxicol. Vitro 24 (2010) 45–55, https://doi.org/10.1016/j.tiv.2009.09.007.

[69] K.-N. Yu, T.-J. Yoon, A. Minai-Tehrani, J.-E. Kim, S.J. Park, M.S. Jeong, S.-W. Ha, J.-K. Lee, J.S. Kim, M.-H. Cho, Zinc oxide nanoparticle induced autophagic cell death and mitochondrial damage via reactive oxygen species generation, Toxicol. Vitro 27 (2013) 1187–1195, https://doi.org/10.1016/j.tiv.2013.02.010.

[70] J.N. D`Souza, G.K. Nagaraja, A. Prabhu, K.M. Navada, S. Kouser, D.J. Manasa, Sauropus androgynus (L.) leaf phytochemical activated biocompatible zinc oxide nanoparticles: an antineoplastic agent against human triple negative breast cancer and a potent nanocatalyst for dye degradation, Appl. Surf. Sci. 552 (2021) 149429, https://doi.org/10.1016/j.apsusc.2021.149429.

[71] H. Yang, C. Liu, D. Yang, H. Zhang, Z. Xi, Comparative study of cytotoxicity, oxidative stress and genotoxicity induced by four typical nanomaterials: the role of particle size, shape and composition, J. Appl. Toxicol. 29 (2009) 69–78, https://doi.org/10.1002/jat.1385.

[72] A. Alamer, D. Ali, S. Alarifi, A. Alkahtane, M. AL-Zharani, M.M. Abdel-Daim, G. Albasher, R. Almeer, N.K. Al-Sultan, A. Almalik, A.H. Alhasan, C. Stournaras, S. Hasnain, S. Alkhatani, Bismuth oxide nanoparticles induce oxidative stress and apoptosis in human breast cancer cells, Environ. Sci. Pollut. Res. 28 (2021) 7379–7389, https://doi.org/10.1007/s11356-020-10913-x.

[73] F. Namvar, H.S. Rahman, R. Mohamad, S. Azizi, P.M. Tahir, M.S. Chartrand, S.K. Yeap, Cytotoxic effects of biosynthesized zinc oxide nanoparticles on murine cell lines, Evid. base Compl. Alternative Med. 2015 (2015) e593014, https://doi.org/10.1155/2015/593014.

[74] Z. Shamasi, A. Es-haghi, M.E. Taghavizadeh Yazdi, M.S. Amiri, M. Homayouni-Tabrizi, Role of Rubia tinctorum in the synthesis of zinc oxide nanoparticles and apoptosis induction in breast cancer cell line, Nanomedicine Journal 8 (2021) 65–72.

[75] V. Valdiglesias, C. Costa, G. Kiliç, S. Costa, E. Pásaro, B. Laffon, J.P. Teixeira, Neuronal cytotoxicity and genotoxicity induced by zinc oxide nanoparticles, Environ. Int. 55 (2013) 92–100, https://doi.org/10.1016/j.envint.2013.02.013.

[76] W.A. Alhoqail, A.S. Alothaim, M. Suhail, D. Iqbal, M. Kamal, M.M. Asmari, A. Jamal, Husk-like zinc oxide nanoparticles induce apoptosis through ROS generation in epidermoid carcinoma cells: effect of incubation period on sol-gel synthesis and anti-cancerous properties, Biomedicines 11 (2023) 320, https://doi.org/10.3390/biomedicines11020320.

[77] P. Mishra, A. Ahmad, L.A. Al-Keridis, N. Alshammari, N.M. Alabdallah, K. Muzammil, M. Saeed, I.A. Ansari, Doxorubicin-conjugated zinc oxide nanoparticles, biogenically synthesised using a fungus Aspergillus Niger, exhibit high therapeutic efficacy against lung cancer cells, Molecules 27 (2022) 2590, https://doi.org/10.3390/molecules27082590.

[78] V. Sharma, D. Anderson, A. Dhawan, Zinc oxide nanoparticles induce oxidative DNA damage and ROS-triggered mitochondria mediated apoptosis in human liver cells (HepG2), Apoptosis 17 (2012) 852–870, https://doi.org/10.1007/s10495-012-0705-6.